Coupled thermodynamic modelling and experimental study of sodium hydroxide activated slag

Zuo, Yibing; Nedeljković, Marija; Ye, Guang

DOI
10.1016/j.conbuildmat.2018.08.087

Publication date
2018

Document Version
Accepted author manuscript

Published in
Construction and Building Materials

Citation (APA)
Zuo, Y., Nedeljković, M., & Ye, G. (2018). Coupled thermodynamic modelling and experimental study of sodium hydroxide activated slag. *Construction and Building Materials*, *188*, 262-279. https://doi.org/10.1016/j.conbuildmat.2018.08.087

Construction and Building Materials, 188(2018) 262-279.

Coupled thermodynamic modelling and experimental study of sodium hydroxide activated slag

Yibing Zuo, Marija Nedeljković, Guang Ye

Section of Materials and Environment, Faculty of Civil Engineering and Geosciences, Delft University of Technology, Stevinweg 1, 2628 CN Delft, The Netherlands

Abstract: In previous researches, the thermodynamic modelling of alkali-activated slag was conducted as a function of the degree of reaction of slag, which makes it difficult to compare the modelling results with the experimental results in a time scale. In this study, the reaction kinetics of sodium hydroxide activated slag was studied using isothermal calorimetry and quantified using the Ginstling-Brounshtein equation. With the quantified reaction kinetics, the hydration of slag was thermodynamically modelled in a time scale. Based on the thermodynamically modelled phase assemblage, chemical shrinkage and phase evolution were derived as a function of time.

Besides the isothermal calorimetry, a series of experimental techniques were used to evaluate the thermodynamic modelling results. Inductively coupled plasma-optical emission spectroscopy (ICP-OES) was used to investigate the pore solution composition. Thermogravimetric analysis (TGA) and X-ray diffraction (XRD) were used to study the reaction products. Energy-dispersive X-ray spectroscopy (EDX) was used to examine the elemental composition of reaction products. The experimental results were presented, discussed, and used to evaluate the thermodynamic modelling results in terms of pore solution composition and reaction products. The modelled pore solution composition matched the experimentally measured data within ±1 order of magnitude. The thermodynamic modelling and experimental results were in agreement regarding bound water, type and amounts of reaction products.

Keywords: NaOH; slag; thermodynamic modelling; reaction kinetics; evaluation

1. Introduction

Thermodynamics plays an important role in the understanding of chemical reactions. It is able to predict whether a reaction can take place and to calculate the solid phase assemblage and the aqueous phase composition at the final state once the reaction is completed. In particular, the thermodynamic modelling has been extensively used in the research of Portland cement hydration [1, 2]. For thermodynamic modelling, it is crucial to obtain the thermodynamic database for the reaction products before performing the thermodynamic calculations. In alkali-activated slag, a calcium-sodium aluminosilicate hydrate (C-(N)-A-S-H) is identified as the primary reaction product [3]. Besides, crystalline reaction products, such as hydrotalcite [4], tetracalcium aluminate hydrate (C_4AH_{13}) [4], katoite (C_3AH_6) [5], and stratlingite (C_2ASH_8) [6], are identified as the secondary reaction products. The thermodynamic data for the secondary reaction products have been reported in the literature [1, 2, 7], such as equilibrium solubility product, enthalpy and entropy etc. However, the thermodynamic data were scarcely determined for C-(N)-A-S-H in the literature. This is because of the amorphous nature of C-(N-)A-S-H and the complex chemical environment (highly alkaline pore solution) in alkali-activated slag. Due to the insufficient thermodynamic data, the hydration of alkali-activated slag is seldom studied via thermodynamic modelling when compared to the hydration of Portland cement.

Lothenbach and Gruskovnjak used a solid solution model to simulate C-(N-)A-S-H in alkali-activated slag [8]. They described C-(N-)A-S-H as a system of two concurrent solid solution systems, based on which the uptake of Al was considered using the Al/Si ratio of 0.1 and the uptake of Na was considered using the ratio of the Na in C-(N-)A-S-H relative to the Na in the aqueous solution. The simulation results showed that the pore solution composition and assemblage of reaction products were consistent with the experimental results in the different alkali-activated slag systems. Later on, this approach was further improved to study the influence

of slag composition in terms of MgO [9] and Al_2O_3 [10] on the hydration of alkali-activated slag. In the approach [9, 10], the uptake of alkalis by C-S-H was modelled by using an ideal solid solution model between jennite, tobermorite, $[(KOH)_{2.5}\cdot SiO_2\cdot H_2O]_{0.2}$ and $[(NaOH)_{2.5}\cdot SiO_2\cdot H_2O]_{0.2}$ as proposed by Kulik et al. in [11]. The uptake of Al by C-S-H was considered based on the energy-dispersive X-ray spectroscopy (EDX) measurement.

For thermodynamic modeling of alkali-activated slag, it is of great significance to account for the uptake of Al and Na into C-S-H. Myers et al. [12], for the very first time, proposed a calcium-alkali aluminosilicate hydrate ideal solid solution model (CNASH_ss) to explicitly account for the structurally-incorporated Al and Na into C-S-H, and applied it to simulate the chemistry of C-(N-)A-S-H in alkali-activated slag. In this approach, a set of eight end-members were used to describe C-(N-)A-S-H based on the sublattice solid solution model. The thermodynamic properties were estimated through the optimization of the equilibrium solubility products for their dissociation reactions. The uptake of Al and Na were considered as an independent substitution in the formation of C-(N)-A-S-H. Afterwards, several researches were carried out using this model to study the hydration of alkali-activated slag.

Myers et al. used the CNASH_ss model to describe the solubility and chemical composition data for C-(N-)A-S-H in sodium silicate and sodium carbonate activated slag [5]. Later on, they used this model to determine the phase diagrams for alkali-activated slag binders with various alkaline activators [13], by which the phase assemblages and chemical properties of these materials can be controlled. By applying the CNASH_ss model, Ye and Radlinska simulated the phase assemblage and chemical shrinkage of alkali-activated slag [14]. However, the aforementioned thermodynamic modelling studies did not take into account the reaction kinetics. As a result, it was not possible to compare the modelling results with the experimental results as a function of

time. For this reason, the reaction degree of slag at a given age has to be approximated before performing thermodynamic modelling.

This study investigated the reaction kinetics of sodium hydroxide activated slag through the measurement of heat evolution rate. The quantification of the reaction kinetics as a function of time was performed by using the Ginstling-Brounshtein equation. The quantified reaction kinetics enabled the correlation between the time and reaction degree of slag, by which the hydration of slag was thermodynamically modelled in a time scale. According to the modelled phase assemblage, chemical shrinkage and phase evolution were derived.

Besides the isothermal calorimetry, a series of experimental techniques were used to study the hydration of slag. Inductively coupled plasma-optical emission spectroscopy (ICP-OES) was used to measure the elemental concentration in the pore solution. Thermogravimetric analysis (TGA) and X-ray diffraction (XRD) were used to study the reaction products. Scanning electron microscopy/energy-dispersive X-ray spectroscopy (SEM/EDX) was used to examine the elemental composition of reaction products. The experimental results were presented nad discussed. By comparing to the experimental data, the thermodynamic modelling results were evaluated in terms of pore solution composition and reaction products. The obtained results contribute to new insights regarding thermodynamic modelling of alkali-activated slag.

2. Materials and methods

2.1. Materials and mixtures

Ground granulated blast furnace slag was used in this study to prepare sodium hydroxide activated slag paste. The chemical composition of slag was determined by X-ray fluorescence spectrometry (XRF) as seen in Table 1. Sodium hydroxide (analytical grade, >98%) was mixed with distilled water to prepare sodium hydroxide activator. The mix compositions of the pastes

are listed in Table 2. The mixtures were denoted as AAS4, AAS6 and AAS8 corresponding to the mixtures with Na_2O/slag = 4%, 6% and 8%, respectively.

Table 1 Chemical composition of blast furnace slag.

Oxide	SiO_2	CaO	Al_2O_3	MgO	Fe_2O_3	SO_3	K_2O	TiO_2	L.I.*
Weight (%)	32.91	40.96	11.85	9.23	0.46	1.61	0.33	1.00	1.15

*L.I. refers to loss on ignition

Table 2 Mix composition of the slag paste per liter.

Mix	Slag (g/L)	Na_2O (g/L)	Water (g/L)
AAS4	1360	54	544
AAS6	1360	82	544
AAS8	1360	109	544

The slag and sodium hydroxide activator were mixed in a commercial Hobart mixer with two minutes low-speed, followed by two minutes high-speed mixing. Subsequently the mixed slag paste was cast into cylinder polyethylene jars (d=35 mm and h=70 mm) and vibrated for 30 s on a vibrating table. All the samples were cured in the closed jars at room temperature until the designed testing age. At the testing age, the samples were crushed into small pieces with dimensions of 1-2 cm^3, and then the small pieces were immersed in isopropanol for at least two weeks to stop reaction of slag. After that, the samples were dried in a vacuum at 20 °C for one week. Then the vacuum dried samples were stored in a desiccator until testing. For the tests of selective dissolution, TGA and XRD, the vacuum dried samples were ground mechanically and manually to reach particle size below 15 μm.

2.2 Test methods

2.2.1. Pore solution analysis via ICP-OES

At the designed testing ages, pore solution of the hardened paste sample was extracted using the steel-die method as described in [15]. Pressures of up to 300 MPa were used to express pore fluid from the samples. After extraction, the pore solution was immediately filtered using Whatman 41 filter paper. One part of the filtered solution was diluted using nitric acid (0.2 vol.%). The diluted

solutions were analyzed using a PerkinElmer Optima 5300DV ICP-OES spectrometer, by which the concentrations of Si, Al, Ca, and Na were determined.

Another part of pore solution was used to determine the concentration of OH^- by titration against hydrochloride acid (0.1 mol/L). Phenolphthalein was used as the indicator. First, a volume (V_1, ml) of pore solution was accurately measured using a pipette and injected into a beaker. Then a drop of phenolphthalein was added into the beaker, and the solution turned red. Afterwards, hydrochloride acid was slowly added into the beaker through a burette until the solution turned colorless (pH<8.2). While adding hydrochloride acid, the beaker was swirled with hand. After the titration, the amount of hydrochloride acid added into the beaker was measured as V_2 (ml). Then the concentration of OH^- ($[OH^-]$, mol/L) could be determined as:

$$[OH^-] = 0.1*V_2/V_1 \quad (1)$$

In the titration test, two replicates of each pore solution were titrated, and the average $[OH^-]$ was presented as the final result.

2.2.2. TGA

TGA measurements were carried out using a heating rate of 10 °C/min from 40 °C to 1000 °C with a thermoanalyzer TG-449-F3-Jupiter instrument. During the measurement, an argon purge of 70 ml/min was applied. The TGA curve provides the weight loss related to the water evaporation or decomposition from the reaction products in the sodium hydroxide activated slag. The weight losses related to C-(N-)A-S-H and hydrotalcite were used to evaluate the thermodynamically modelled bound water in C-(N-)A-S-H and hydrotalcite.

2.2.3. XRD

XRD analysis was performed on the powdered samples using a Philips X'Pert diffractometer applying CuK_α radiation (λ = 1.54 Å). The samples were scanned between 5° and 70° 2-theta, with a step size of 0.02° 2-theta and a dwell time of 5 s per step. In order to determine the

amounts of different phases in sodium hydroxide activated slag, silicon was added as an internal standard to replace 10% of sodium hydroxide activated slag sample. Through the Rietveld analysis method [16], the proportions of different phases were determined.

2.2.4. SEM/EDX

The vacuum dried samples were impregnated using a low viscosity epoxy resin and then polished down to ¼ μm [17]. The polished samples were examined for the observations of microstructure and the elemental compositions of the reaction products using a Philips XL30 SEM equipped with NSS3.3. The EDX measurements were carried out at an accelerating voltage of 15 kV in the high vacuum mode. Before the measurements, the polished samples were carbon coated. A total of 30 points (EDX spots) per sample at each studied age were analyzed. It is noted that corrections were employed using ZAF method in the EDX measurement [18]. The aim of ZAF method is to convert apparent concentrations (raw peak intensity) into (semi-quantitative) concentrations corrected to eliminate inter-element matrix effects. For a clear observation of the microstructure, the micrographs were taken at an accelerating voltage of 20 kV in the low vacuum mode.

2.2.5. Isothermal calorimetry

The reaction kinetics of sodium hydroxide activated slag was studied using isothermal calorimetry. The isothermal calorimetry measurements were carried out in accordance with ASTM C1679 [19]. For the measurement of heat evolution, external mixing was used. Prior to sample preparation, slag and sodium hydroxide activators were conditioned at 20 °C. After mixing slag with alkaline activator externally, the fresh paste was immediately placed into the calorimeter. Two replicates were measured simultaneously. The heat flow was recorded and the cumulative heat was calculated up to 7 days.

2.2.6. Selective dissolution

It is reported that salicylic acid-methanol (SAM) dissolves calcium silicate hydrates but is not supposed to dissolve the unreacted slag [20, 21]. Many researchers have used the selective dissolution by SAM to determine the reaction degree of alkali-activated slag [22, 23]. In this study, 1 g of powdered sodium hydroxide activated slag sample was added to a solution containing 4 g of salicylic acid mixed in 60 ml of methanol. The mixture was stirred for 2 h and the suspension was then vacuum filtered in a fume hood. Afterwards, the insoluble residue was placed into a crucible and ignited in a furnace at 1000 °C for 30 min. After ignition, the mass of the insoluble residue was recorded as m_1. In the meantime, 1 g of powdered sodium hydroxide activated slag sample was also ignited in the furnace to determine the total amount of slag (m_0). As such, the reaction degree of slag (α) can be determined using Eq. (2).

$$\alpha = \frac{m_0 - m_1}{m_0} \qquad (2)$$

It is noted that the determination of reaction degree through Eq. (2) did not take into account the correction for hydrotalcite. However, this would not affect the results. The details will be further discussed in Section 3.5.2.

2.3. Quantification of reaction kinetics

Similar to the hydration of Portland cement, the reaction of alkali-activated slag also experiences several different reaction stages that are controlled by different reaction mechanisms. The reaction process of alkali-activated slag usually consists of initial dissolution period, induction period, acceleration/deceleration period and steady period [24]. The occurrence of induction period depends on the type of alkaline activator. The reaction stages of sodium hydroxide activated slag in this study will be further discussed in Section 3.5.1. In the literature, several reaction models are used to describe the reaction kinetics as a function of time.

The model as described in Eq. (3) [25], can be used to determine the reaction degree if the rate of glass dissolution is controlled by a chemical reaction.

$$1-\left(1-\alpha(t)\right)^{1/3}=K_1 t \qquad (3)$$

Where $K_1 = k_1/r_0$ with k_1 being a rate constant and r_0 being the initial radius of a sphere, and $\alpha(t)$ is the reaction degree at time t. However, the formation of reaction products around slag grains results in diffusion as the dominant rate controlling process in the hydration of alkali-activated slag, especially in a later age. Therefore, Eq. (3) is not suitable to describe the reaction degree of alkali-activated slag.

The Jander's model, originally developed for diffusion controlled reactions in solid state sintering [26], is given by Eq. (4).

$$\left[1-(1-\alpha(t))^{1/3}\right]^2=K_2\cdot t \qquad (4)$$

Where $K_2 = k_2/R^2$ with k_2 being a diffusion constant and R being the initial radius of a reacting sphere. Based on Eq. (4), Eq. (5) introduces a reaction grade *N* for a broader application, i.e. to model consecutive and sometimes overlapping reaction processes [26-28].

$$\left[1-(1-\alpha(t))^{1/3}\right]^N=K_2\cdot t \qquad (5)$$

However, the Jander's model was based on a fundamentally flawed mathematical derivation. This is because the particle surface curvature was neglected when substituting the $\alpha(t)$ defined in spherical coordinates into the diffusion-controlled equation defined in Cartesian coordinates [29]. For this reason, the Jander equations (Eq. (4) and Eq. (5)) are strictly not correct and thus not suitable for use in describing the cement hydration and quantifying the reaction kinetics.

Using the steady-state solution of Fick's first law, Eq. (6) was developed, also known as the Ginstling-Brounshtein equation [30].

$$1-\frac{2}{3}\alpha(t)-(1-\alpha(t))^{2/3}=k\cdot t \qquad (6)$$

Where $k = D \cdot C_2 \cdot \mu/(\rho \cdot n)$. D is the diffusion coefficient of the reactant, C_2 is the concentration of the reactant at the surface, μ is the molecular weight and ρ is the density of the reaction products, and n is the stoichiometric coefficient of the reaction. Since the derivation of Ginstling-Brounshtein equation is carried out in spherical coordinates [29], it correctly accounts for particle surface curvature.

The calorimetric responses of sodium hydroxide activated slag (see Fig. 9) indicate different mechanism-controlled reaction kinetics besides the diffusion controlled reaction kinetic. In order to describe the whole reaction process, a reaction grade *N* was introduced into the Ginstling-Brounshtein equation as follows:

$$\left[1-\frac{2}{3}\alpha(t)-(1-\alpha(t))^{2/3}\right]^{N}=k\cdot t \qquad (7)$$

or in its linear form:

$$\ln\left[1-\frac{2}{3}\alpha(t)-(1-\alpha(t))^{2/3}\right]=\frac{1}{N}\ln k+\frac{1}{N}\ln t \qquad (8)$$

The reaction grade *N* indicates the reaction rate controlling mechanism [27, 28]. When $N<1$, reaction occurs through the nucleation kinetic; when *N* is close to 1, reaction occurs through the phase-boundary kinetic; when *N* is close to 2, reaction occurs through the diffusion kinetic. In this study, Eq. (7) (or Eq. (8)) was used to quantify the reaction kinetics of sodium hydroxide activated slag.

2.4. Thermodynamic modelling

The CNASH_ss model proposed by Myers et al. [12] was used in this study. Among the eight end-members for C-(N-)A-S-H, 5CA and INFCA are two C-A-S-H end-members, 5CNA and INFCNA are two C-N-A-S-H end-members, INFCN is a C-N-S-H end-member, and T2C*, T5C* and TobH* are three C-S-H end-members. The MA-OH-LDH model [12], consisting of three end-members (M_4AH_{10}, M_6AH_{12}, M_8AH_{14}), was used to model the hydrotalcite-like phases. The

chemical reactions and equilibrium solubility products of the eight end-members for C-(N-)A-S-H and the three end-members for hydrotalcite-like phases were reproduced in Table 3.

In the calculations of Myers et al. [5, 12], Fe was not considered due to its very low content in slag and sulfur was represented as S^{2-}. According to Wolthers et al. [31], disordered mackinawite is the first iron sulfide to form in most ambient environments, and with time it reacts to form more stable iron sulfide phases such as ordered mackinawite and ultimately pyrite or pyrrhotite. It was reported that mackinawite is more stable in the alkali-activated slag system than other phases like Fe-ettringite or microcrystalline $Fe(OH)_3$ [8]. In this study, mackinawite was included to consider the reactions between aqueous Fe^{2+} and S^{2-} under ambient conditions. More details on the thermodynamic properties of other secondary reaction products can be referred to [5].

Table 3 Chemical reactions and equilibrium solubility products at 25 ℃ and 1 bar for C-(N-)A-S-H and hydrotalcite-like phases

End-member	Chemical reactions	*Log K*
C-(N-)A-S-H gel ideal solid solution eight end-members, 'CNASH_ss' model [12]		
5CA	$(CaO)_{1.25}\cdot(Al_2O_3)_{0.125}\cdot(SiO_2)\cdot(H_2O)_{1.625} \Leftrightarrow 1.25Ca^{2+} + SiO_3^{2-} + 0.25AlO_2^- + 0.25OH^- + 1.5H_2O$	-10.75
INFCA	$(CaO)\cdot(Al_2O_3)_{0.15625}\cdot(SiO_2)_{1.1875}\cdot(H_2O)_{1.65625} + 0.6875OH^- \Leftrightarrow Ca^{2+} + 1.1875SiO_3^{2-} + 0.3125AlO_2^- + 2H_2O$	-8.90
5CNA	$(CaO)_{1.25}\cdot(Na_2O)_{0.25}\cdot(Al_2O_3)_{0.125}\cdot(SiO_2)\cdot(H_2O)_{1.25} \Leftrightarrow 1.25Ca^{2+} + SiO_3^{2-} + 0.25AlO_2^- + 0.5Na^+ + 0.75OH^- + H_2O$	-10.40
INFCNA	$(CaO)\cdot(Na_2O)_{0.34375}\cdot(Al_2O_3)_{0.15625}\cdot(SiO_2)_{1.1875}\cdot(H_2O)_{1.3} \Leftrightarrow Ca^{2+} + 1.1875SiO_3^{2-} + 0.3125AlO_2^- + 0.6875Na^+ + 1.3125H_2O$	-10.00
INFCN	$(CaO)\cdot(Na_2O)_{0.3125}\cdot(SiO_2)_{1.5}\cdot(H_2O)_{1.1875} + 0.375OH^- \Leftrightarrow Ca^{2+} + 1.5SiO_3^{2-} + 0.625Na^+ + 1.375H_2O$	-10.70
T2C*	$(CaO)_{1.5}\cdot(SiO_2)\cdot(H_2O)_{2.5} \Leftrightarrow 1.5Ca^{2+} + SiO_3^{2-} + 0H^- + 2H_2O$	-11.60
T5C*	$(CaO)_{1.25}\cdot(SiO_2)_{1.25}\cdot(H_2O)_{2.} \Leftrightarrow 1.25Ca^{2+} + 1.25SiO_3^{2-} + 2.5H_2O$	-10.50
TobH*	$(CaO)\cdot(SiO_2)_{1.5}\cdot(H_2O)_{2.5} + 0H^- \Leftrightarrow Ca^{2+} + 1.5SiO_3^{2-} + 3H_2O$	-7.90
MA-OH-LDH ideal solid solution three end-members, 'MA-OH-LDH _ss' model [12]		
M_4AH_{10}	$(MgO)_4\cdot(Al_2O_3)\cdot(H_2O)_{10} \Leftrightarrow 4Mg^{2+} + 2AlO_2^- + 6OH^- + 7H_2O$	-49.70
M_6AH_{12}	$(MgO)_6\cdot(Al_2O_3)\cdot(H_2O)_{12} \Leftrightarrow 6Mg^{2+} + 2AlO_2^- + 10OH^- + 7H_2O$	-72.02
M_8AH_{14}	$(MgO)_8\cdot(Al_2O_3)\cdot(H_2O)_{14} \Leftrightarrow 8Mg^{2+} + 2AlO_2^- + 14OH^- + 7H_2O$	-94.34

The thermodynamic modelling for AAS4, AAS6 and AAS8 was carried out in an N_2 atmosphere at 25 °C, 1 bar using GEM-Selektor V3 (http://gems.web.psi.ch/) [32, 33]. The thermodynamic database was described in [5, 12], which is based on an updated version of CEMDATA07 [34].

This thermodynamic database contains the CNASH_ss model for C-(N-)A-S-H gel and MA-OH-LDH model for hydrotalcite-like phases. As it is directly encoded in GEM-Selektor, the extended Debye-Huckel equation is used to calculate the ion activity coefficients [32, 33]. The extended Debye-Huckel equation is accurate at moderate ionic strengths (up to ~1-2 molal) [35], which is lower than the ionic strength in the pore solutions of alkali-activated slag (~1-3 molal in sodium silicate activated slag [36]). However, use of an improved aqueous phases model, such as the Pitzer model [37], is limited in the current version of GEM-Selektor. This is because the description of aqueous silicate species in the database of GEM-Selektor does not extend beyond dimeric silicate and aluminosilicate units [12]. On the other hand, GEM-Selektor has been commonly used in the thermodynamic modelling of alkali-activated slag, and the modelling results agreed well with the experimental data [5, 13, 38]. As such, slight excess of ionic strengths (> 2 molal) would not impose a serious impact on the modelling results.

In thermodynamic modelling, congruent slag dissolution was assumed and proportional additions of SiO_2, CaO, Al_2O_3, MgO, Fe_2O_3, H_2S and K_2O were used. This is reasonable for the dissolution of aluminosilicate glass in alkaline solution [39]. It is worth noting that the samples were cured at 20 °C in experiments, which is slightly different from the standard equilibrium temperature. However, this difference does not have a significant influence on the rate of diffusion or the stability of minerals [34], and hence would not impose a significant impact on the equilibrium solubility products and the thermodynamic modeling results.

3. Results and discussion

3.1. Pore solution composition analyzed by ICP-OES

Fig.1 presents the measured concentrations of Si, Al, OH^-, Ca and Na (hereafter denoted as [Si], [Al], [OH^-] and [Na] respectively) in the pore solution of sodium hydroxide activated slag paste as a function of time up to 28 days (672 hours).

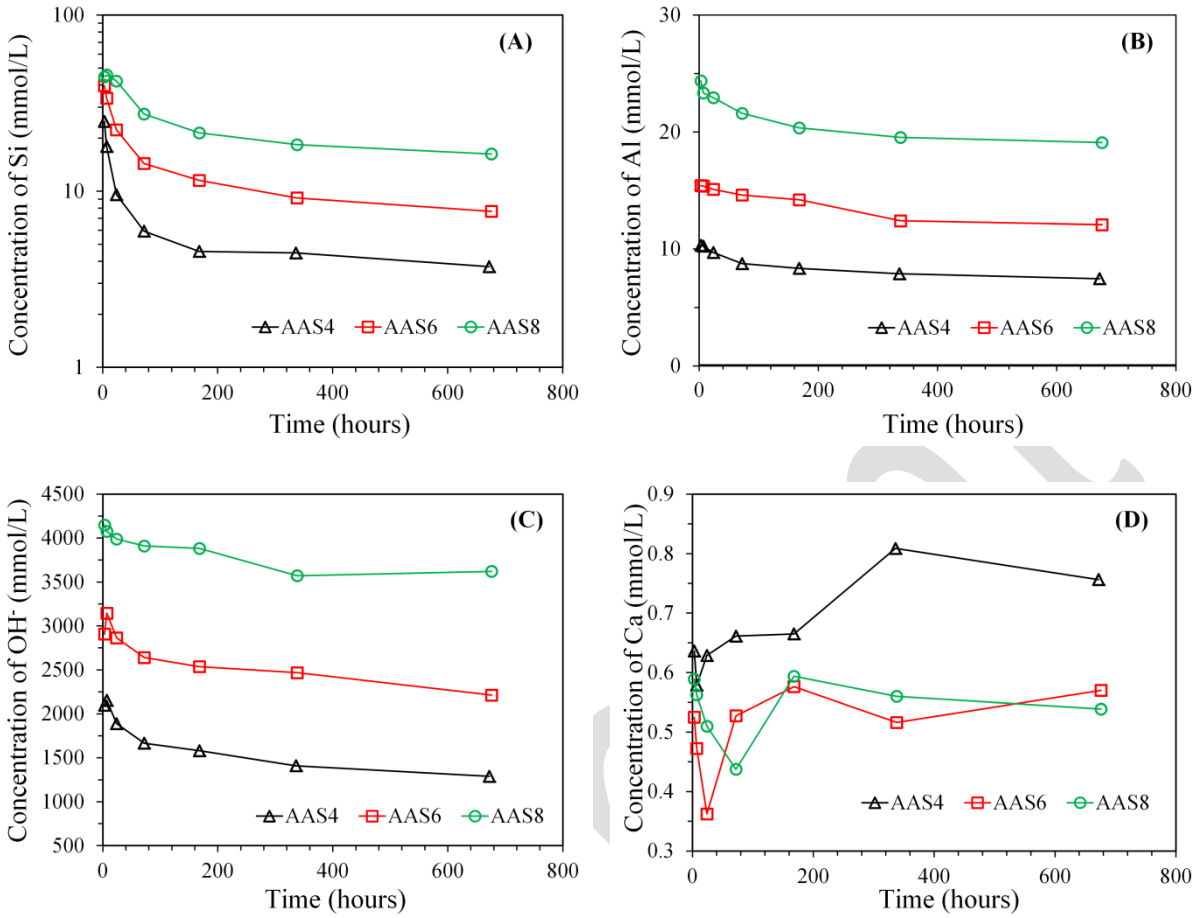

Fig. 1. Elemental concentrations measured by ICP-OES analysis technique. (A) [Si]; (B) [Al]; (C) [OH^-]; (D) [Ca] and (E) [Na]. In the graphs, AAS indicates alkali-activated slag, and the number following AAS refers to the weight percentage of Na_2O with respect to slag. Water to slag ratio was 0.4 and the curing temperature was 20 °C.

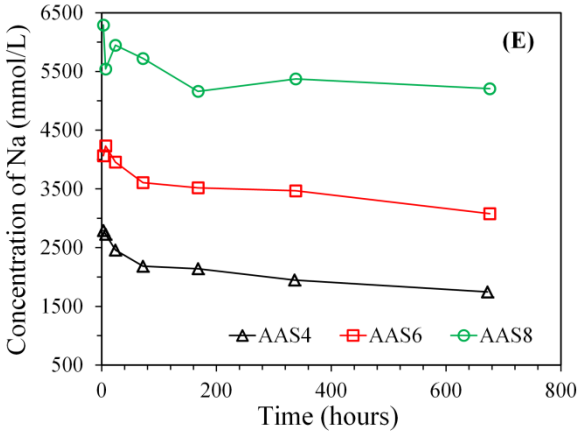

The pore solution composition was dominated by Na and OH^-, whereas much lower concentrations of Si, Al and Ca were observed. The most significant changes in the compositions of pore solutions in sodium hydroxide activated slag pastes occurred during the first hours up to 3 days. This can be seen from the changes of elemental concentrations with time, particularly the

decreases of [Si] (Fig. 1(A)), [Na] (Fig. 1(E)) and [OH^-] (Fig. 1(C)). Except for the concentration of Ca, all other elemental concentrations increased with the increase of Na_2O content from 4% to 8%. The concentrations of Si, Al and Ca were in the order: [Si] > [Al] > [Ca].

The [OH^-] indicated a pH within the range of 14.11~14.62 up to 28 days in the pore solution, showing a higher alkalinity than that in the pore solution (pH>12) buffered by $Ca(OH)_2$ in OPC-based materials [40]. Compared to the concentration of Na, the [OH^-] was about 20-30 % smaller. Regarding this difference, two reasons may explain. On one hand, [Na] was measured by ICP-OES analysis technique, while [OH^-] was determined by titration against hydrochloride acid. In the titration test, pore solution was titrated to a pH below 8.2 when the solution color turned from red to colorless. After termination of the titration, the solution was still basic and OH^- ions were not completely titrated. As such, the measured [OH^-] was underestimated. On the other hand, many other anions were present in the pore solution besides OH^-, such as SiO_3^{2-}, AlO_2^-, S^{2-} and HS^- etc. Since the pore solution was electrically neutral, the presence of other anions would lead to smaller [OH^-] than [Na].

In pore solutions, the concentration of Ca remained at a very low level and slightly decreased as the concentration of OH^- increased. This could be attributed to the common ion effect [41, 42]. The pore solutions had high concentrations of Si, OH^- and Na^+. Those ions might combine with Ca to form solid reaction products and thus lowered the Ca concentration in the pore solution. Therefore, [Ca] stayed on a low concentration and the increase of [OH^-] led to a decrease of [Ca] in the pore solution.

3.2. Thermogravimetric analysis

The weight loss and differential thermogravimetric data (DTG) are presented in Fig. 2 for AAS4, AAS6 and AAS8 at 1, 7 and 28 days. The DTG curve indicated the presence of C-(N-)A-S-H and hydrotalcite for all the sodium hydroxide activated slag samples, which is consistent with the

observations reported in [9, 10, 17]. Katoite loses its water at 320 °C [43], but it was not identified from the DTG curve in this work.

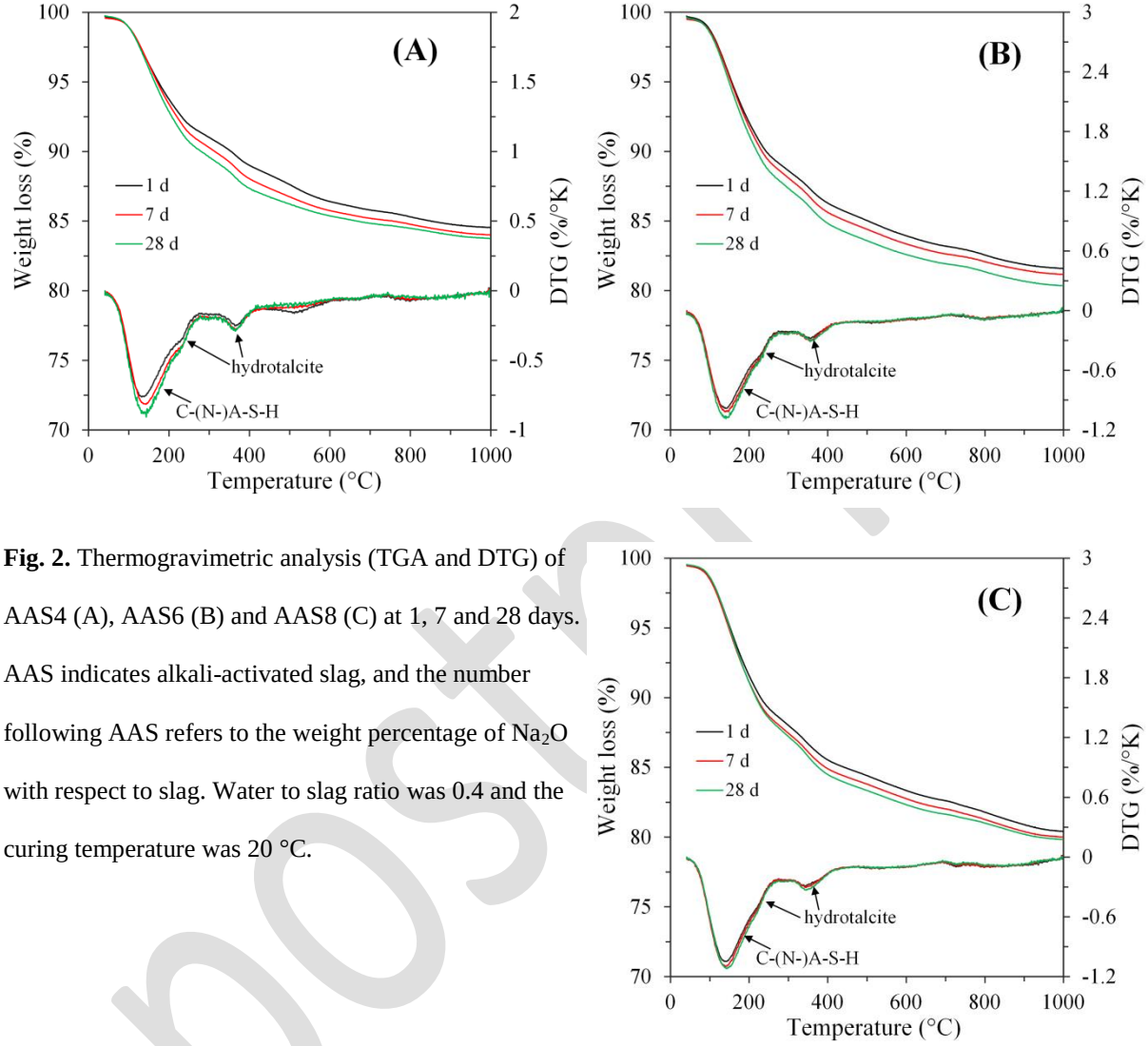

Fig. 2. Thermogravimetric analysis (TGA and DTG) of AAS4 (A), AAS6 (B) and AAS8 (C) at 1, 7 and 28 days. AAS indicates alkali-activated slag, and the number following AAS refers to the weight percentage of Na_2O with respect to slag. Water to slag ratio was 0.4 and the curing temperature was 20 °C.

Portlandite was detected by XRD (only in AAS8, see Section 3.3) and thermodynamic modelling (see Section 3.6), but it was not identified from the DTG curve. Two reasons may explain this discrepancy. On one hand, the amount of portlandite was very small according to XRD and thermodynamic modelling results. As such, the weight loss due to the bound water release from portlandite was very small, and thus it might be below the detection limit. On the other hand, the water loss of portlandite at around 460 °C is close to the water loss of hydrotalcite at around

400 °C [43]. According to XRD and thermodynamic modelling, a large amount of hydrotalcite formed in sodium hydroxide activated slag. As such, a broad shoulder at around 400 °C was detected on the DTG curve as seen in Fig. 2. The broad shoulder may cover the weight loss that came from the water release from portlandite. Those two aspects could lead to absence of the peaks that correspond to portlandite from the DTG curve.

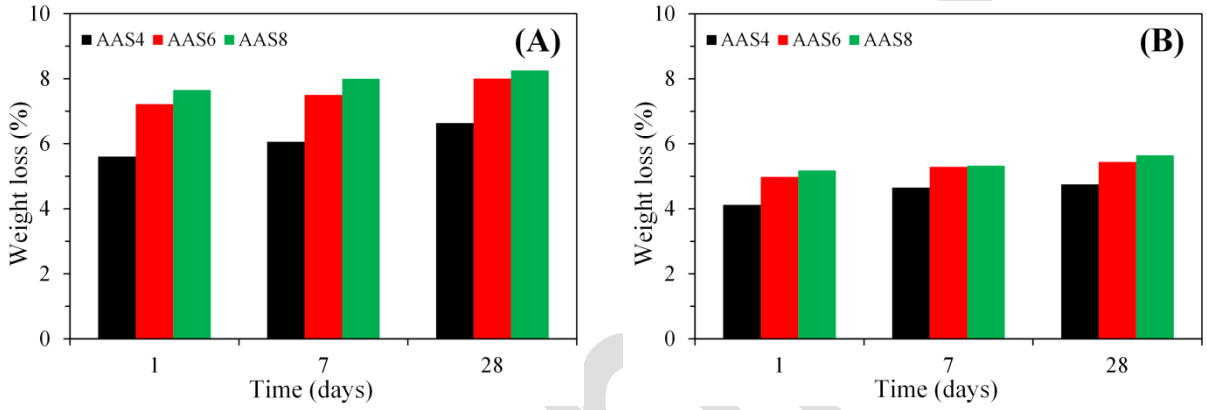

Fig. 3. Weight loss from TGA in the temperature ranges of 105 °C - 215 °C (A) and 215 °C - 400 °C (B). In the graphs, AAS indicates alkali-activated slag, and the number following AAS refers to the weight percentage of Na_2O with respect to slag. Water to slag ratio was 0.4 and the curing temperature was 20 °C.

The weight loss from 40 °C to 105 °C is mostly due to the evaporable water in the sample. From 105 °C to 215 °C, the weight loss is mainly attributed to the loss of bound water in C-(N-)A-S-H, while from 215 °C to 400 °C, it is mainly resulted from the release of bound water from hydrotalcite. The weight losses in the temperature ranges of 105 °C - 215 °C and 215 °C - 400 °C are shown in Fig. 3 for AAS4, AAS6 and AAS8 at 1, 7 and 28 days. The weight loss in the temperature range of 105 °C - 215 °C increased with time, indicating increasing amount of C-(N-)A-S-H formed with time. It can also be seen that the increase of Na_2O content led to the increase of weight loss from 105 °C - 215 °C, suggesting increasing amount of C-(N-)A-S-H formed in the sample. It is noted that similar observations were also found for the weight loss from 215 °C to 400 °C that the weight loss slightly increased with increases of curing time and Na_2O content.

This indicates that the amount of hydrotalcite formed in the sample increased slightly with the increases of curing time and Na_2O content.

3.3. X-ray diffraction

Fig. 4 shows the XRD patterns of raw slag and AAS4, AAS6 and AAS8 at 1, 7 and 28 days. The XRD pattern of raw slag shows that it is fully amorphous. In all sodium hydroxide activated slag samples, hydrotalcite and katoite were identified, which is consistent with the previous studies [4, 14, 44]. It is noted that portlandite was only detected in AAS8. The presence of portlandite in sodium hydroxide activated slag was also reported in the literature [14].

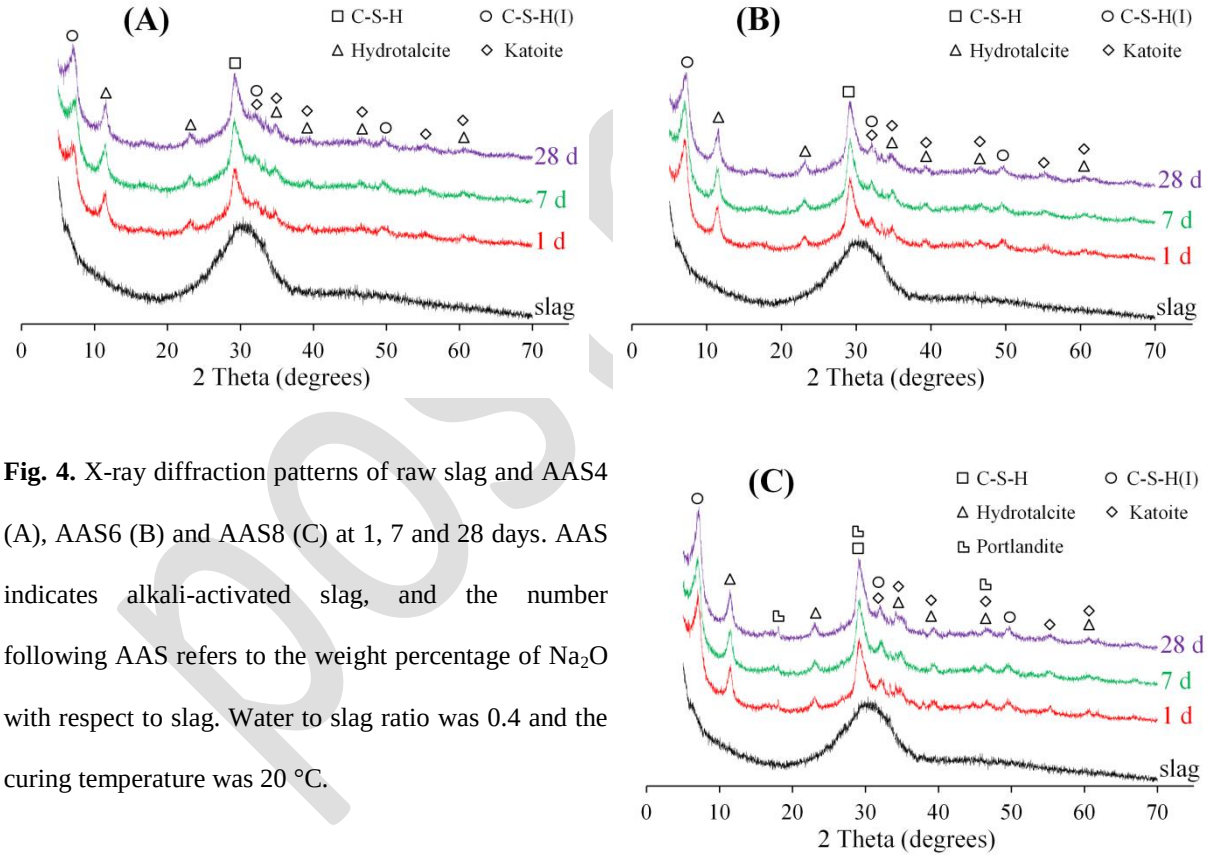

Fig. 4. X-ray diffraction patterns of raw slag and AAS4 (A), AAS6 (B) and AAS8 (C) at 1, 7 and 28 days. AAS indicates alkali-activated slag, and the number following AAS refers to the weight percentage of Na_2O with respect to slag. Water to slag ratio was 0.4 and the curing temperature was 20 °C.

The diffusive peaks at $2\theta = 29.07°$ were dominant in all sodium hydroxide activated slag samples. These diffusive peaks are associated with the calcium silicate hydrates (C-S-H) [9, 14]. According to the previous studies [4, 9, 14], the peaks at approximately $2\theta = 7.0°$, 32.0° and 49.8°

are attributed to the poorly crystalline C-S-H(I). The poorly crystalline C-S-H(I) is considered more ordered than the C-S-H in ordinary Portland cement paste at ambient temperature [45] and has been commonly observed in concrete containing pozzolans and also in alkali-activated slag [46]. It can be seen that longer curing time and increase of Na_2O content led to increase of intensity and sharper shape of the peaks corresponding to C-S-H(I). This indicates that the crystallinity of C-S-H(I) increased with increases of curing time and Na_2O content.

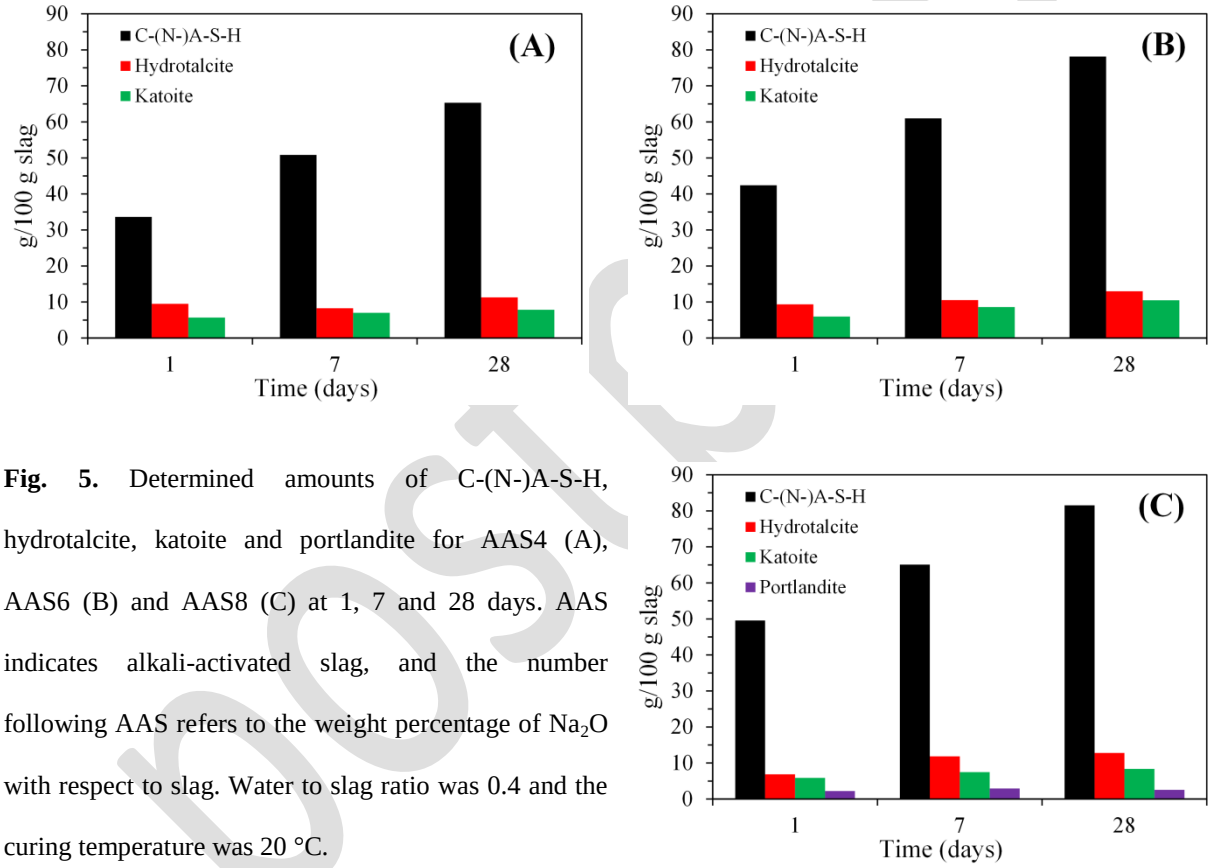

Fig. 5. Determined amounts of C-(N-)A-S-H, hydrotalcite, katoite and portlandite for AAS4 (A), AAS6 (B) and AAS8 (C) at 1, 7 and 28 days. AAS indicates alkali-activated slag, and the number following AAS refers to the weight percentage of Na_2O with respect to slag. Water to slag ratio was 0.4 and the curing temperature was 20 °C.

The amounts of crystalline reaction products (hydrotalcite, katoite and portlandite) were determined using Rietveld method. By subtracting the crystalline reaction products, the amount of amorphous phases can be calculated. In the hydrated slag, the amorphous phases consist of unreacted slag and C-(N-)A-S-H. Based on the quantified reaction kinetics in Section 3.5.2, the amount of unreacted slag can be determined at any given age. By subtracting the amount of

unreacted slag from the total amount of amorphous phases, the amount of C-(N-)A-S-H was calculated. Fig. 5 presents the determined amounts of C-(N-)A-S-H, hydrotalcite, katoite and portlandite using Rietveld method coupled with the quantified reaction kinetics. It is noted that the unit of per 100 g slag refers to 100 g of slag mixed originally, instead of slag reacted or unreacted, throughout the whole text.

It can be seen that C-(N-)A-S-H was the dominant phase in the reaction products for all sodium hydroxide slag samples. The amount of C-(N-)A-S-H increased with the increases of curing time and Na_2O content. The increase of curing time also led to increasing amounts of hydrotalcite and katoite for all sodium hydroxide slag samples, while it did not show much influence on the amount of portlandite in AAS8. The determined amounts of C-(N-)A-S-H and crystalline reaction products will be used to evaluate the thermodynamically modelled results in Section 3.7.3.

3.4. SEM/EDX microanalysis

Fig. 6 shows the SEM-micrographs of AAS4, AAS6 and AAS8 at 1 d. It can be seen that for all the samples, grey reaction products containing C-(N-)A-S-H and crystalline reaction products surrounded the bright unreacted slag particles. As Na_2O content increased from 4% to 8%, the sodium hydroxide activated slag sample exhibited a larger volume of reaction products and hence a denser microstructure. By image analysis [47], the area fraction of reaction products was calculated as 54.8%, 68.6%, and 74.3% for AAS4, AAS6, and AAS8 respectively at 1 day. The increasing amount of reaction products with increase of the Na_2O content agreed with the TGA and XRD-Rietveld results.

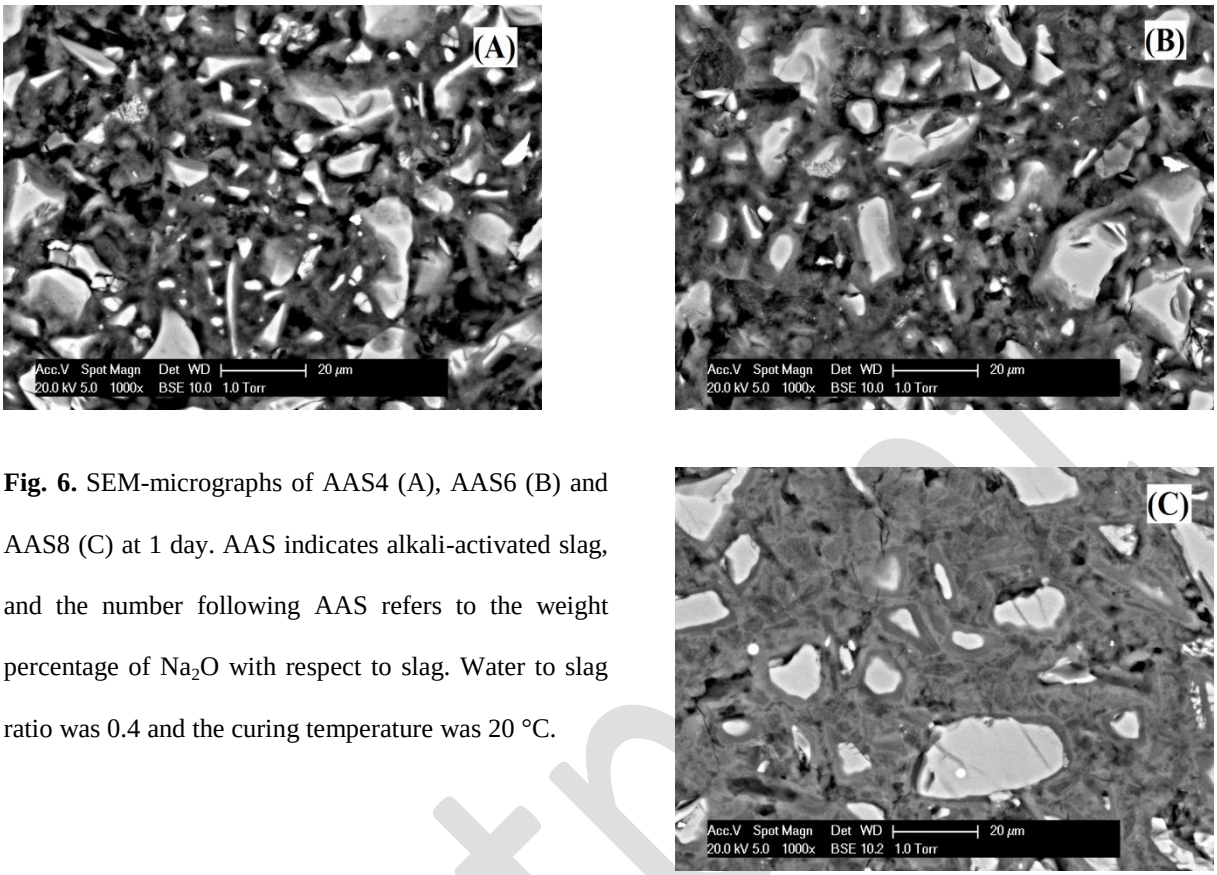

Fig. 6. SEM-micrographs of AAS4 (A), AAS6 (B) and AAS8 (C) at 1 day. AAS indicates alkali-activated slag, and the number following AAS refers to the weight percentage of Na_2O with respect to slag. Water to slag ratio was 0.4 and the curing temperature was 20 °C.

In the EDX data acquisition, the size of the interaction volume between electron and specimen is a few microns for cementitious materials [43]. The measured EDX results actually represent the chemical composition of solid phases within the interaction volume. In alkali-activated slag, the secondary reaction products are often intimately intermixed with C-(N-)A-S-H [48, 49]. As such, the influence of possible presence of secondary reaction products should be taken into account when interpreting the measurements.

Based on the EDX measured data, the overall atomic ratios Al/Ca versus Si/Ca are presented in Fig. 7 for AAS4, AAS6 and AAS8 at 1, 7 and 28 days. The positions of possible reaction products were marked, such as C_3AH_6, C_2ASH_8, and $Ca(OH)_2$. The clusters marked with circles are assumed as C-(N-)A-S-H. It is clear that C-(N-)A-S-H was not the only phase that was explored by EDX. C_3AH_6, C_2ASH_8, and $Ca(OH)_2$ are all likely to be present in these materials.

For example, the data points locating between the stoichiometric values of Si/Ca and Al/Ca for C_3AH_6 and those for C-(N-)A-S-H indicated the potential presence of C_3AH_6.

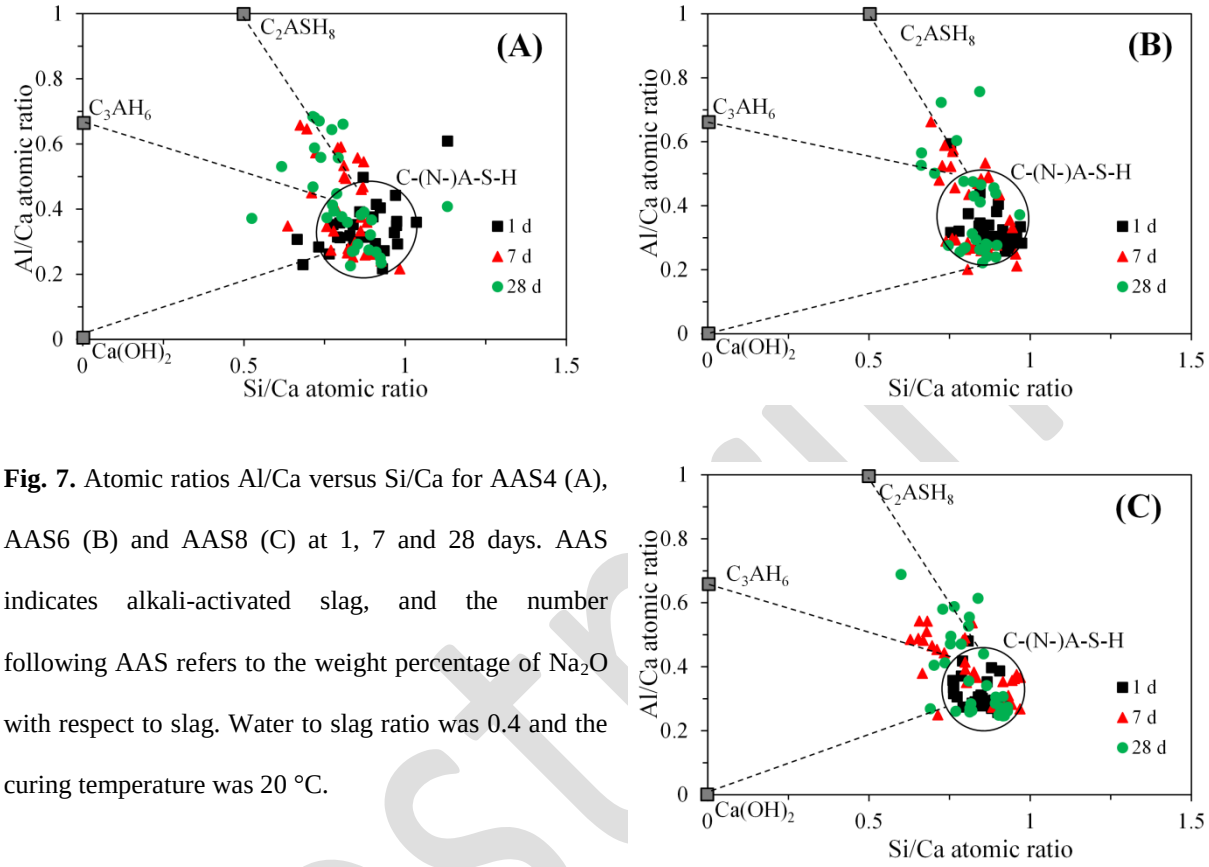

Fig. 7. Atomic ratios Al/Ca versus Si/Ca for AAS4 (A), AAS6 (B) and AAS8 (C) at 1, 7 and 28 days. AAS indicates alkali-activated slag, and the number following AAS refers to the weight percentage of Na_2O with respect to slag. Water to slag ratio was 0.4 and the curing temperature was 20 °C.

Fig. 8 presents the overall atomic ratios Mg/Si versus Al/Si for AAS4, AAS6 and AAS8 at 1, 7 and 28 days. Regardless of the curing time, a quasi-linear relationship was observed between Mg/Si and Al/Si. As seen in Fig. 8, this quasi-linear relationship was fitted and represented by a black line. According to the previous studies [9, 10, 50], the slope of the fitted line indicates the Mg/Al ratio in hydrotalcite and the intercept of the fitted line in the Al-Si axis indicates the uptake of Al by C-S-H phases. The regressed equations show the Mg/Al ratios of 2.26, 2.44 and 2.99 for AAS4, AAS6 and AAS8 respectively. These Mg/Al ratios are well within the range of 1.92 to 4.35 reported for hydrated slag pastes [45, 51, 52]. The intercepts of the fitted lines in the

Al-Si axis were calculated as 0.22, 0.25 and 0.27, indicating the uptake of Al by C-S-H for AAS4, AAS6 and AAS8 respectively.

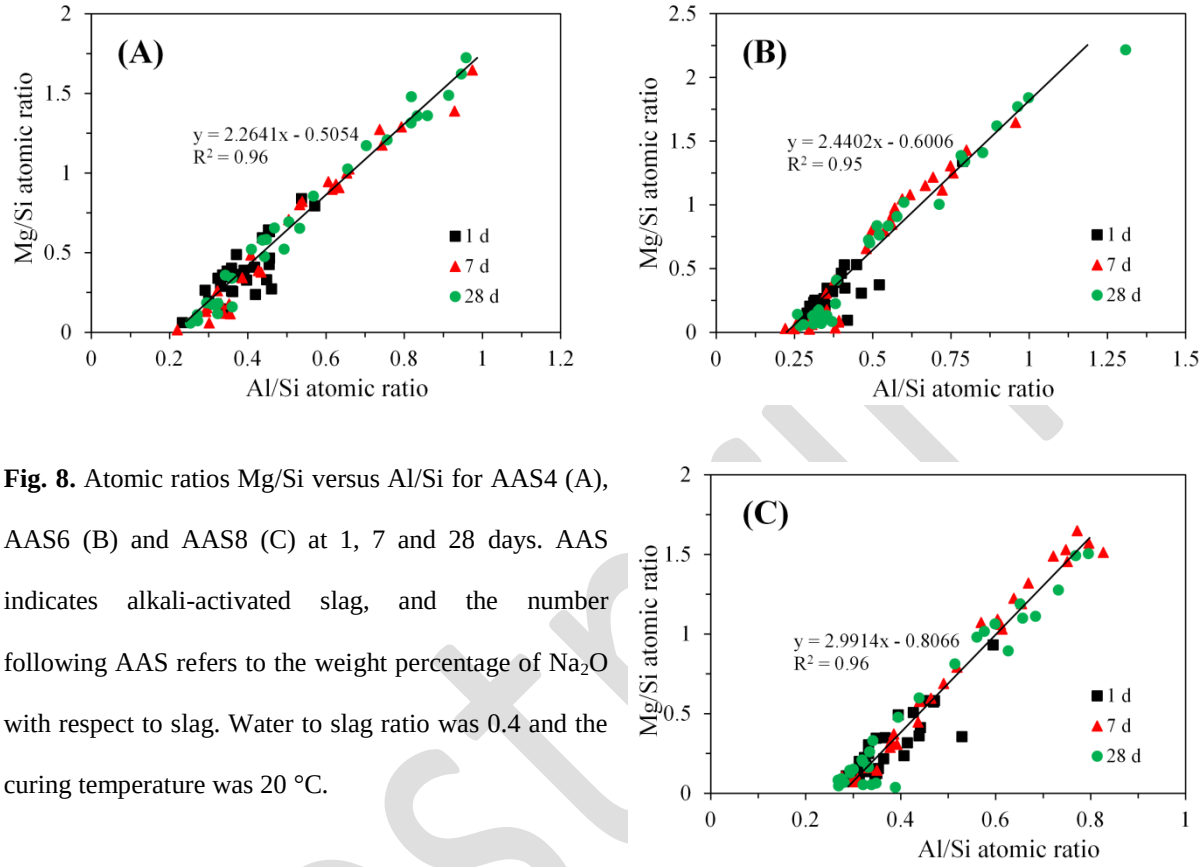

Fig. 8. Atomic ratios Mg/Si versus Al/Si for AAS4 (A), AAS6 (B) and AAS8 (C) at 1, 7 and 28 days. AAS indicates alkali-activated slag, and the number following AAS refers to the weight percentage of Na_2O with respect to slag. Water to slag ratio was 0.4 and the curing temperature was 20 °C.

3.5. Reaction kinetics

3.5.1. Isothermal calorimetry investigations

The calorimetric responses of sodium hydroxide activated slag are presented in Fig. 9; Fig. 9(A) shows the heat evolution rate and Fig. 9(B) shows the cumulative heat release over the first 168 h for AAS4, AAS6 and AAS8. Two calorimetric peaks were observed from the heat evolution rate curves, which agrees with the observations in [22, 24, 26, 53, 54]. The first peak (P_1) with significant high heat flow within the first 10 min corresponds to the dissolution/wetting of slag after mixing with alkaline activator [22, 26]. The second peak (P_2) occurred between 1 h and 3 h

is assigned to the formation of a large amount of reaction products [22, 24]. According to those two calorimetric peaks, the entire reaction process of sodium hydroxide activated slag can be divided into three reaction stages, namely initial dissolution period (I), acceleration/deceleration period (II) and steady period (III). In comparison with the four distinctive reaction stages (dissolution, induction, acceleration/deceleration and steady state) in the hydration process of a normal Portland cement [45], no noticeable induction period was observed in the hydration process of sodium hydroxide activated slag.

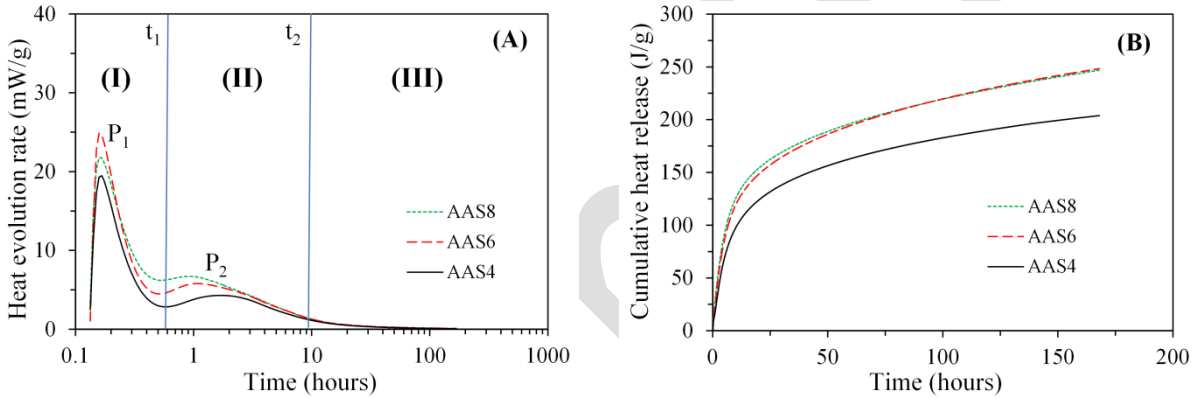

Fig. 9. Heat evolution rate (A) and cumulative heat release (B) of sodium hydroxide activated slag. Time t_1 and t_2 are the transition time and the representative vertical dividing lines are shown for AAS4. P_1 and P_2 are the first and second calorimetric peak respectively. In the graphs, AAS indicates alkali-activated slag, and the number following AAS refers to the weight percentage of Na_2O with respect to slag. Water to slag ratio was 0.4 and the curing temperature was 20 °C.

The magnitude of acceleration peak (i.e., the second calorimetric peak) was influenced by the content of Na_2O. The height of acceleration peak increased when the content of Na_2O increased from 4% to 8%. Increment of Na_2O content increased the alkalinity of sodium hydroxide activator, accelerating the dissolution of slag and thus the formation of reaction products. Consequently, the height of acceleration peak increased and its appearance occurred earlier. The cumulative heat release curves for sodium hydroxide activated slag pastes (Fig. 9(B)) indicated

more heat release with increasing Na_2O content. However, further more addition of Na_2O beyond 6% did not show an obvious influence on the cumulative heat.

3.5.2. Quantification of reaction kinetics using the Ginstling-Brounshtein equation

Based on the cumulative heat release (Fig. 9(B)), the reaction degree of slag (α(t)) can be calculated using Eq. (9).

$$\alpha(t) = \frac{Q(t)}{Q_{max}} \quad (9)$$

Where Q(t) is the cumulative heat release at time t and Q_{max} is the total heat release. In order to obtain the total heat release, the reaction degree at 7 days was determined using the SAM selective dissolution method (see Section 2.2.2). The reason to select the determination of reaction degree at 7 days is because the heat release of sodium hydroxide activated slag already became weak and stable at 7 days. Given the reaction degree and cumulative heat release at 7 days, the total heat release can be obtained using Eq. (9). The calculation results are listed in Table 4. The calculated total heat release is very close to the reported value of 460 J/g slag in the literature [55]. Given the total heat release, the reaction degree was calculated as a function of time using Eq. (9), and plotted in Fig. 10 for AAS4, AAS6 and AAS8.

Table 4 Total amount of slag (m_0) and amount of unreacted slag (m_1) in 1 g vacuum dried sample at 7 days. Reaction degree and cumulative heat release at 7 days, and total heat release

Sample	m_0 (g)	m_1 (g)	α	Q(J/g slag)	Q_{max} (J/g slag)
AAS4	0.846	0.440	0.48	203.8	425.1
AAS6	0.811	0.349	0.57	248.3	436.2
AAS8	0.799	0.325	0.59	246.8	415.8

The reaction degrees at 7 days determined by SE-image analysis [47] were also presented in Fig. 10. The reaction degrees at 7 days determined by SAM selective dissolution are comparable to those results obtained by SE-image analysis. This suggests good quality of the results determined by SAM selective dissolution without correction for hydrotalcite.

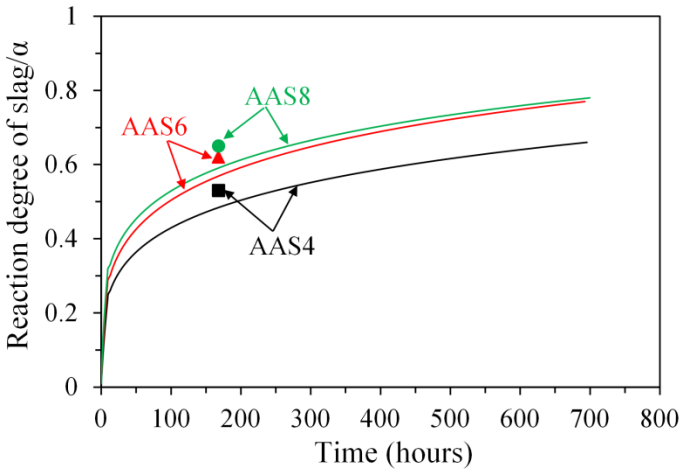

Fig. 10. Reaction degree of slag as a function of time for sodium hydroxide activated slag. The solid lines were derived according to Eq. (9), and the dots were obtained by SE-image analysis [47]. In the graphs, AAS indicates alkali-activated slag, and the number following AAS refers to the weight percentage of Na_2O with respect to slag. Water to slag ratio was 0.4 and the curing temperature was 20 °C.

The heat evolution rate curve (Fig. 9(A)) indicates three reaction stages during the reaction process of sodium hydroxide activated slag. At each reaction stage, the linear relationship between ln[1-2α/3-(1- α)2/3] and ln*t* (see Eq. (8)) was regressed as shown in Fig. 11. The slope and intercept of the linear relationship are 1/*N* and ln*k*/*N* respectively. Based on the regressed equations, the slope and intercept were determined. Given the slope and intercept, the reaction grade (*N*) and rate parameter (*k*) were calculated. The calculation results are listed in Table 5. Given *N* and *k*, the reaction kinetics of sodium hydroxide activated slag can be quantified as a function of time using Eq. (7).

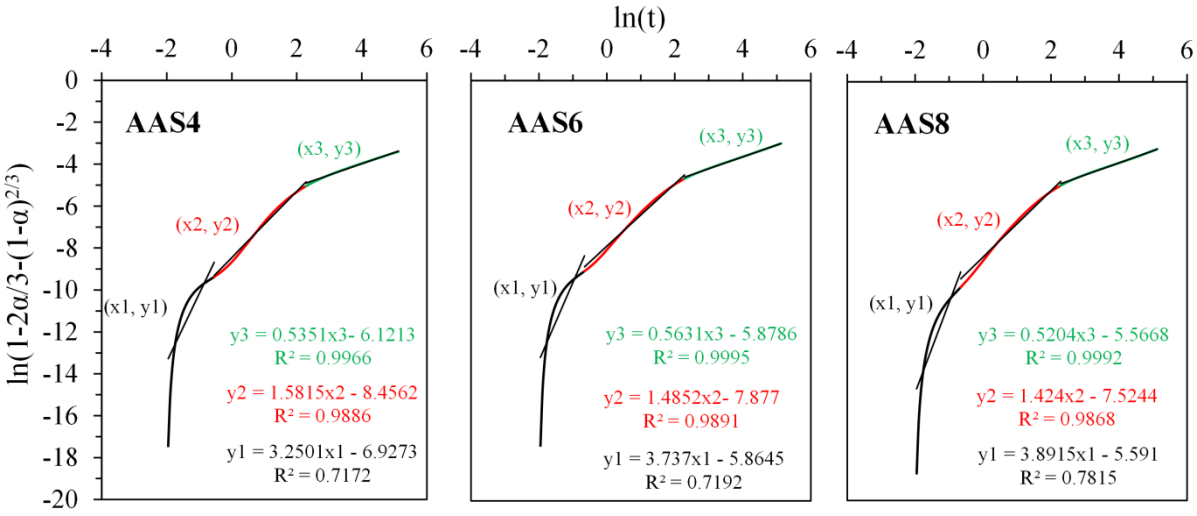

Fig. 11. Linear fits applied to ln[1-2α/3-(1- α)2/3] versus ln*t* relationship for sodium hydroxide activated slag. (x1, y1), (x2, y2) and (x3, y3) correspond to the initial dissolution period, acceleration/deceleration period and steady period respectively. In the graphs, AAS indicates alkali-activated slag, and the number following AAS refers to the weight percentage of Na_2O with respect to slag. Water to slag ratio was 0.4 and the curing temperature was 20 °C.

Table 5 Transition time, reaction grade and rate parameter

Sample	Transition time (hour)		1st reaction stage		2nd reaction stage		3rd reaction stage	
	t_1	t_2	*N*	*k*	*N*	*k*	*N*	*k*
AAS4	0.58	9.82	0.31	0.12	0.63	0.0048	1.87	1.08E-05
AAS6	0.52	9.82	0.27	0.21	0.67	0.0050	1.78	2.92E-05
AAS8	0.52	9.82	0.26	0.24	0.70	0.0051	1.92	2.26E-05

The N values in Table 5 suggest that reaction of slag experienced three reaction stages that were controlled by different reaction mechanisms. In the first reaction stage, the reaction process of slag was controlled by the nucleation kinetic. In the second reaction stage, the reaction process of slag was most likely controlled by the phase-boundary kinetic. In the last reaction stage, the reaction process of slag was controlled by the diffusion kinetic. As seen in Table 5, k generally increased with the increase of Na_2O content. This indicates a faster reaction rate for the reaction of sodium hydroxide activated slag with a higher content of Na_2O. These results are in line with the calorimetric data.

3.6. Thermodynamic modelling in a time scale

With the quantified reaction kinetics as a function of time, the hydration of sodium hydroxide activated slag was thermodynamically modelled in a time scale. Fig. 12 presents the modelled solid phase assemblages of sodium hydroxide activated slag as a function of time.

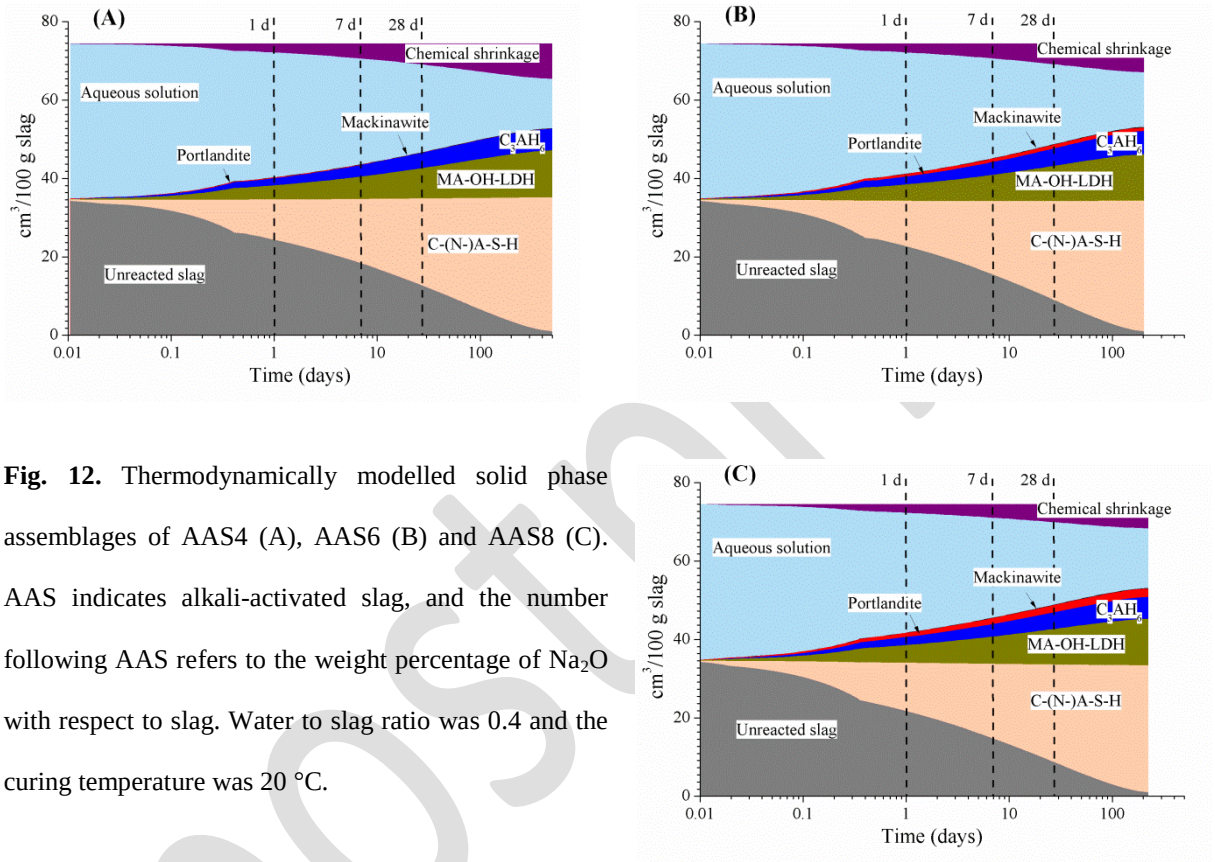

Fig. 12. Thermodynamically modelled solid phase assemblages of AAS4 (A), AAS6 (B) and AAS8 (C). AAS indicates alkali-activated slag, and the number following AAS refers to the weight percentage of Na_2O with respect to slag. Water to slag ratio was 0.4 and the curing temperature was 20 °C.

For all sodium hydroxide activated slag samples, the modelling results suggest formation of C-(N-)A-S-H as the primary reaction products and the formation of hydrotalcite-like phases (MA-OH-LDH), katoite (C_3AH_6), portlandite and mackinawite as the secondary reaction products. It can be also seen that Na_2O content in the range of 4% to 8% did not impose much influence on the solid phase assemblages except for the portlandite formation. In AAS4, only trace amount of portlandite was formed before 7 d, while in AAS6 and AAS8, evolution of portlandite increased with time. Based on the modelled phase assemblages, some properties can be calculated as a

function of time, such as the volume ratio between reaction products and reacted slag, volume fraction of C-(N-)A-S-H in total reaction products, and chemical shrinkage. The time-dependent thermodynamic modelling results enable convenient and direct comparisons with the experimental results.

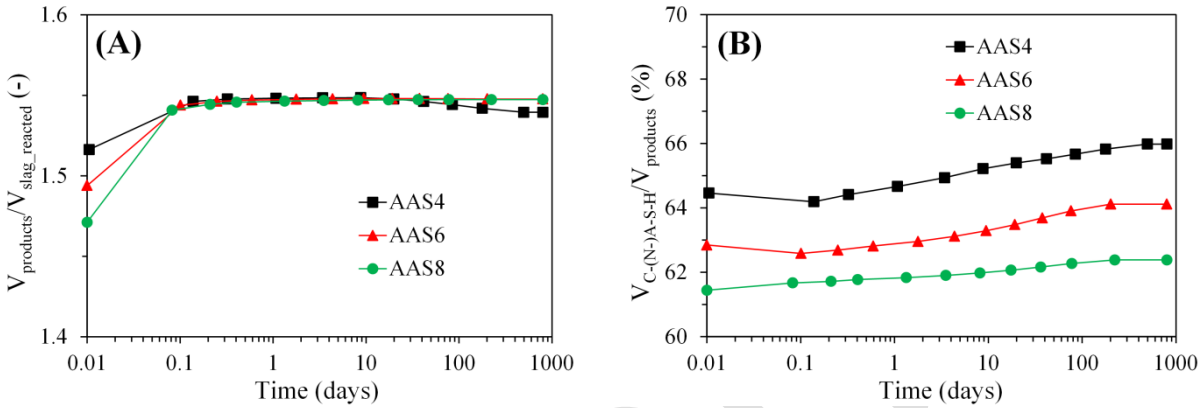

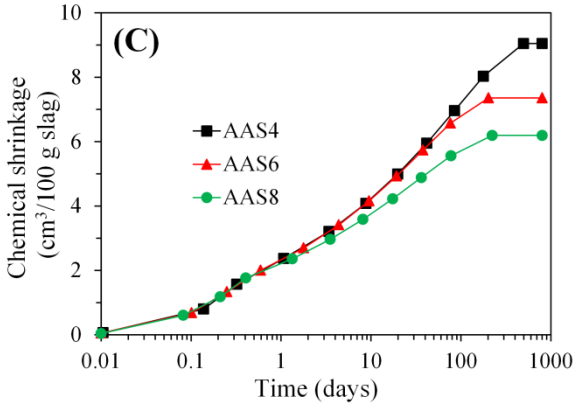

Fig. 13. Thermodynamic modelling results in a time scale: (A) Volume ratio $V_{products}/V_{slag\_reacted}$, (B) volume fraction $V_{C-(N-)A-S-H}/V_{products}$ and (C) chemical shrinkage in volume (cm^3) per 100 gram of slag mixed. In the graphs, AAS indicates alkali-activated slag, and the number following AAS refers to the weight percentage of Na_2O with respect to slag. Water to slag ratio was 0.4 and the curing temperature was 20 °C.

The ratio between the volume of reaction products ($V_{products}$) and the volume of reacted slag ($V_{slag\_reacted}$) is presented in Fig. 13(A). The volume ratio ($V_{products}$/ $V_{slag\_reacted}$) represents the pore space filling capacity by solid phases. In Portland cement, this volume ratio is reported from 2.06 to 2.2 [56]. As seen in Fig. 13(A), it fell between 1.45 and 1.55 for sodium hydroxide activated slag, which is much smaller than the value reported for Portland cement. This volume ratio increased in the beginning few hours and then stayed at around 1.54 till the complete hydration of

slag. It seems that the Na_2O content did not have an obvious impact on the volume ratio after the beginning few hours.

Fig. 13(B) shows that the volume fraction of primary reaction products ($V_{C\text{-}(N\text{-})A\text{-}S\text{-}H}$) in the total reaction products ($V_{products}$) was between 60% and 67%. This indicates that C-(N-)A-S-H contributed 20~34% more to the volumetric solid phase growth than the secondary reaction products. On one hand, the volume fraction of C-(N-)A-S-H increased slightly with time. On the other hand, the volume fraction of C-(N-)A-S-H decreased with the increase of Na_2O content. This is because a higher content of Na_2O increased the polymerization degree of C-(N-)A-S-H and thus led to a higher density of C-(N-)A-S-H [17]. So, Na_2O has an obvious influence on the contribution of C-(N-)A-S-H to the solid phase growth by volume.

As a function of time, the chemical shrinkage per 100 g of slag mixed (instead of slag reacted) is presented in Fig. 13(C). It can be seen that the chemical shrinkage increased with time, and decreased with increase of Na_2O content. Compared to the experimental measurements in the literature [14], the results predicted by thermodynamic modelling were less sensitive to the concentration of sodium hydroxide activators. The chemical shrinkage of Portland cement at complete hydration is reported to be approximately 6.4 cm^3/100 g [57, 58]. When slag is completely reacted, the predicted chemical shrinkage by thermodynamic modelling was 9.1, 7.4 and 6.2 cm^3/100 g slag for AAS4, AAS6 and AAS8 respectively. These predicted values are relatively smaller than the chemical shrinkage quantified experimentally by Thomas et al. for a sodium silicate activated slag (12.2±1.5 cm^3/100 g slag) [59], and the values modelled by Chen and Brouwers (11.5-13.7 cm^3/100 g slag) [60] at complete reaction of slag. This difference was attributed to the different slags and alkaline activators used in the literature and the current work. It is reported that the differences in slag and alkaline activator can result in different chemical shrinkage at complete reaction of slag [14, 60, 61].

The chemical shrinkage at complete reaction of slag decreased with increase of Na_2O content, which is in agreement with the experimental finding [61]. This phenomenon can be explained in two aspects. On one hand, the increase of Na_2O content led to a higher alkalinity of sodium hydroxide activator, which resulted in a higher polymerization degree of C-(N-)A-S-H [62]. The higher polymerization degree of C-(N-)A-S-H reduced the amount of water retained in C-(N-)A-S-H [17]. This can be evidenced by thermodynamic modelling in Fig. 15(A). At 100% degree of reaction of slag, the predicted amount of water retained in C-(N-)A-S-H was 15.6, 14.3 and 13.0 g/100 g slag for AAS4, AAS6 and AAS8 respectively. Then the reduced retained water in C-(N-)A-S-H reduced the chemical shrinkage [60]. On the other hand, the increase of Na_2O content led to decrease of the amount of C-(N-)A-S-H produced at complete relation of slag as seen in Figs. 12 and 13(B). The reduced amount of C-(N-)A-S-H also reduced the chemical shrinkage. When it was expressed in volume fraction in the system, the chemical shrinkage was 0.12, 0.099 and 0.083 for AAS4, AAS6 and AAS8 respectively at 100 % degree of reaction of slag. The value of 0.12 for AAS4 is smaller than the value of 0.15 reported for sodium silicate activated slag with the same content of Na_2O and water/slag ratio [38]. The sodium hydroxide activator has a higher alkalinity than the sodium silicate activator when they have the same contents of Na_2O and water [63]. The higher alkalinity of sodium hydroxide activator in this work causes a higher polymerization degree of C-(N-)A-S-H and thus results in a smaller chemical shrinkage in comparison with the sodium silicate activated slag in [38]. It can be concluded that the chemical shrinkage at complete reaction of slag is dependent on the content of Na_2O in alkaline activator as well as the type of alkaline activator.

3.7. Evaluation of the thermodynamic modelling results by comparing to the experimental measurements

In this section, the thermodynamic modelling results in terms of pore solution composition, bound water, amounts of reaction products and elemental composition of reaction products, were presented, and evaluated by comparing to the experimental results. By performing the thermodynamic modelling using GEM-Selektor V3 [32, 33], the concentration of element in aqueous solution and mol amounts of reaction products can be directly obtained from the output. According to the mol amounts of C-(N-)A-S-H and hydrotalcite, their mass amounts, bound water and elemental composition were calculated.

3.7.1. Pore solution composition

The thermodynamically modelled elemental concentrations in comparison with the experimental results are plotted as a function of time in Fig. 14. It can be seen that the modelled elemental concentrations show a good agreement with the experimental results in the altering trend with time, particularly for the concentrations of Si, Al, Na and OH^-. The modelled concentrations of Al and Na agree well the measured values. It is noted that the modelled concentration of OH^- only consisted of the free OH^-. Since a large amount of aqueous sodium hydroxide (NaOH(aq)) were present in the aqueous solution of sodium hydroxide activated slag, the concentration of the collected free OH^- was very low when compared to the concentration of Na. As seen in Fig. 14 (F) for the modelled concentrations versus the experimental concentrations regardless of time and Na_2O content, the modelled results matched the experimentally measured data within ± 1 order of magnitude. Mostly, the modelled results underestimated the elemental concentrations, particularly for the concentrations of Si (Fig. 14(A)) and Ca (Fig. 14(D)). This phenomena will be explained in the following paragraph.

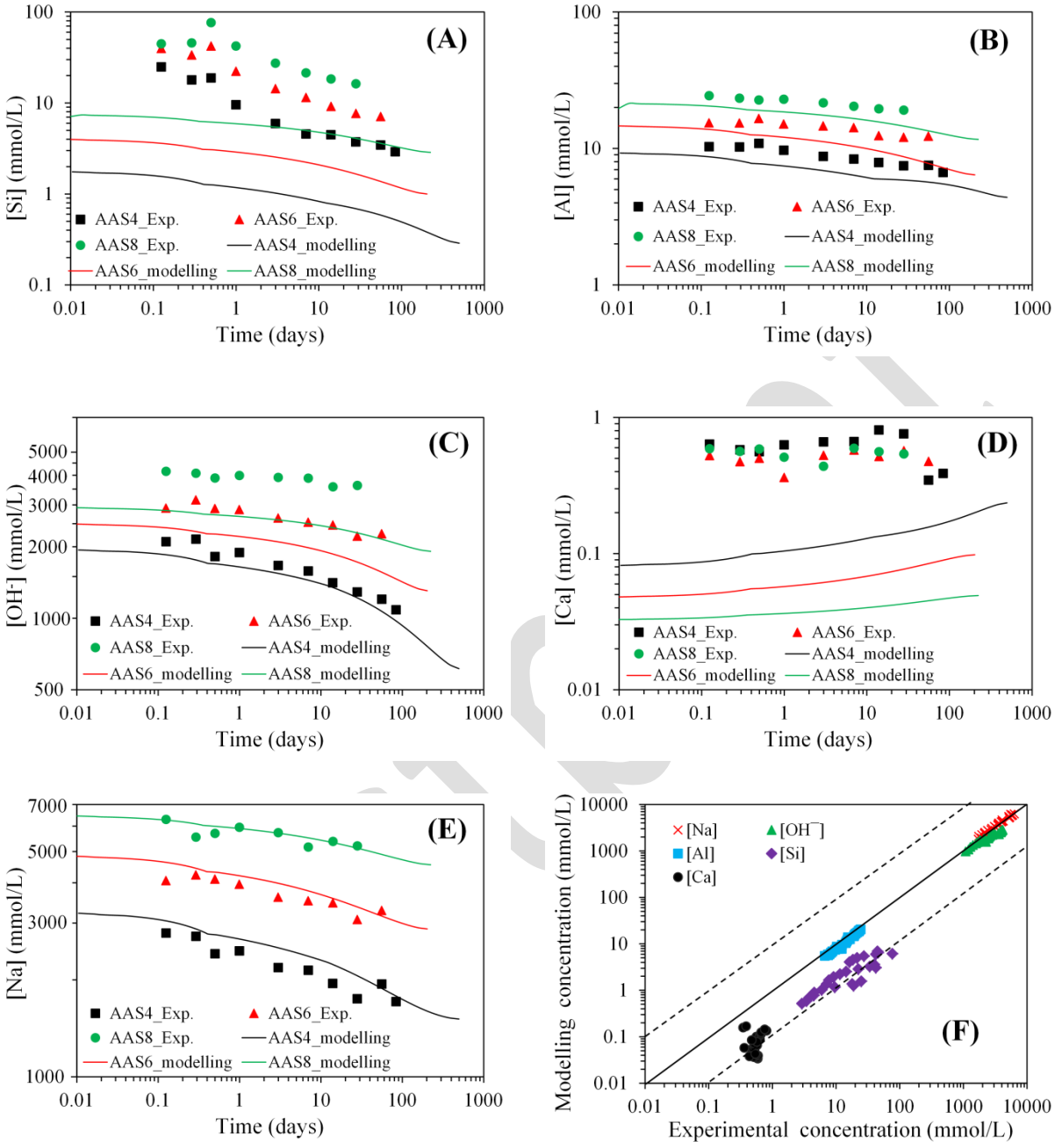

Fig. 14. Modelled elemental concentrations in comparison with the experimental measurements. (A) [Si]; (B) [Al]; (C) [OH^-]; (D) [Ca], (E) [Na] and (F) modelling concentration versus experimental concentration regardless of time and Na_2O content. In the graphs, AAS indicates alkali-activated slag, and the number following AAS refers to the weight percentage of Na_2O with respect to slag. Exp. is abbreviated from experimental. Water to slag ratio was 0.4 and the curing temperature was 20 °C.

1

In thermodynamic modelling, thermodynamic equilibriums are assumed between the aqueous ions in the aqueous solution and the solid reaction products. However, the pore solution of sodium hydroxide activated slag is actually oversaturated with respect to solid reaction products with time [64]. For clear discussion, the aqueous ions are presumed to be divided into two parts. The first part are the aqueous ions that are in thermodynamic equilibriums with the solid reaction products, and the second part are the aqueous ions that result in oversaturation with respect to the solid reaction products. The assumption of thermodynamic equilibriums in thermodynamic modelling causes the second part of aqueous ions to be completely reacted to form solid reaction products and only leaves the first part of aqueous ions in the solution. As a result, the thermodynamic modelling results underestimate the elemental concentrations in the pore solution. Because C-(N-)A-S-H is the primary reaction product and it mainly consists of Si and Ca tetrahedras, so the underestimation by thermodynamic modelling is strongly reflected on the concentrations of Si and Ca.

3.7.2. Bound water in C-(N-)A-S-H and hydrotalcite per 100 gram of slag mixed

As seen in Fig. 2, most of the bound water in C-(N-)A-S-H and hydrotalcite were lost from 105 °C to 215 °C and from 215 °C to 400 °C respectively. So this study assumed the weight losses from 105 °C to 215 °C and from 215 °C to 400 °C as the bound water in C-(N-)A-S-H and hydrotalcite respectively, to evaluate the thermodynamically modelled bound water in these reaction products. Fig. 15 plots the modelled amounts of bound water in comparison with TGA results as a function of time for C-(N-)A-S-H and hydrotalcite. The comparisons show good agreements between the modelled amounts of bound water and the measured ones in the altering trend with time. The agreement became better when curing time increased from 1 d to 7 days, particularly for the amount of bound water in hydrotalcite after 7 days.

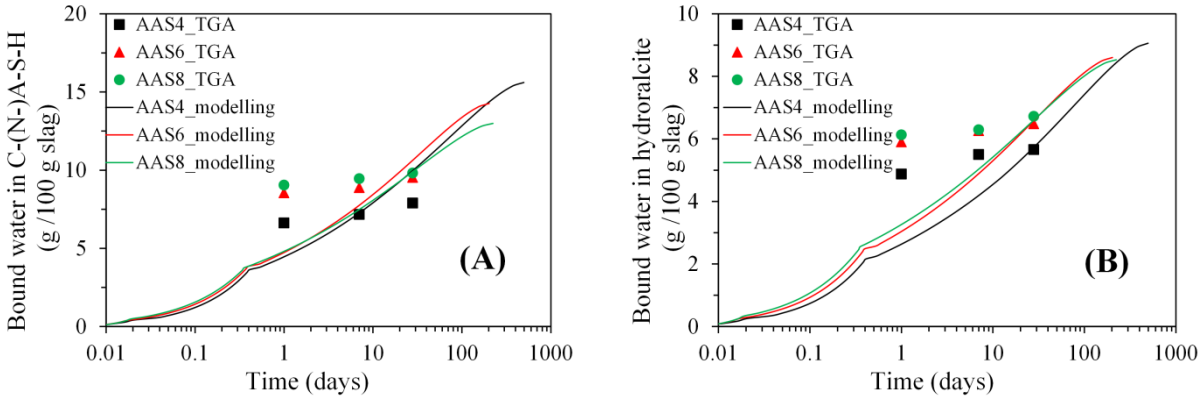

Fig. 15. Modelled amounts of bound water in comparison with TGA results as functions of time. (A) bound water in C-(N-)A-S-H, (B) bound water in hydrotalcite. In the graphs, AAS indicates alkali-activated slag, and the number following AAS refers to the weight percentage of Na_2O with respect to slag. Water to slag ratio was 0.4 and the curing temperature was 20 °C.

3.7.3. Reaction products per 100 gram of slag mixed

The thermodynamically modelled amounts of reaction products in comparison with the XRD results are presented as a function of time in Fig. 16. Fig. 16(A) suggests a good agreement in the altering trend with time between the modelled amounts of C-(N-)A-S-H and the measured results. Both the modelling and XRD results show that the amount of C-(N-)A-S-H increased with the increment of Na_2O content. Fig. 16(B) and Fig. 16(C) present the modelled amounts of hydrotalcite and katoite respectively in comparison with the measured data. It can be seen that the modelled amounts of hydrotalcite and katoite agreed well with the experimentally measured results.

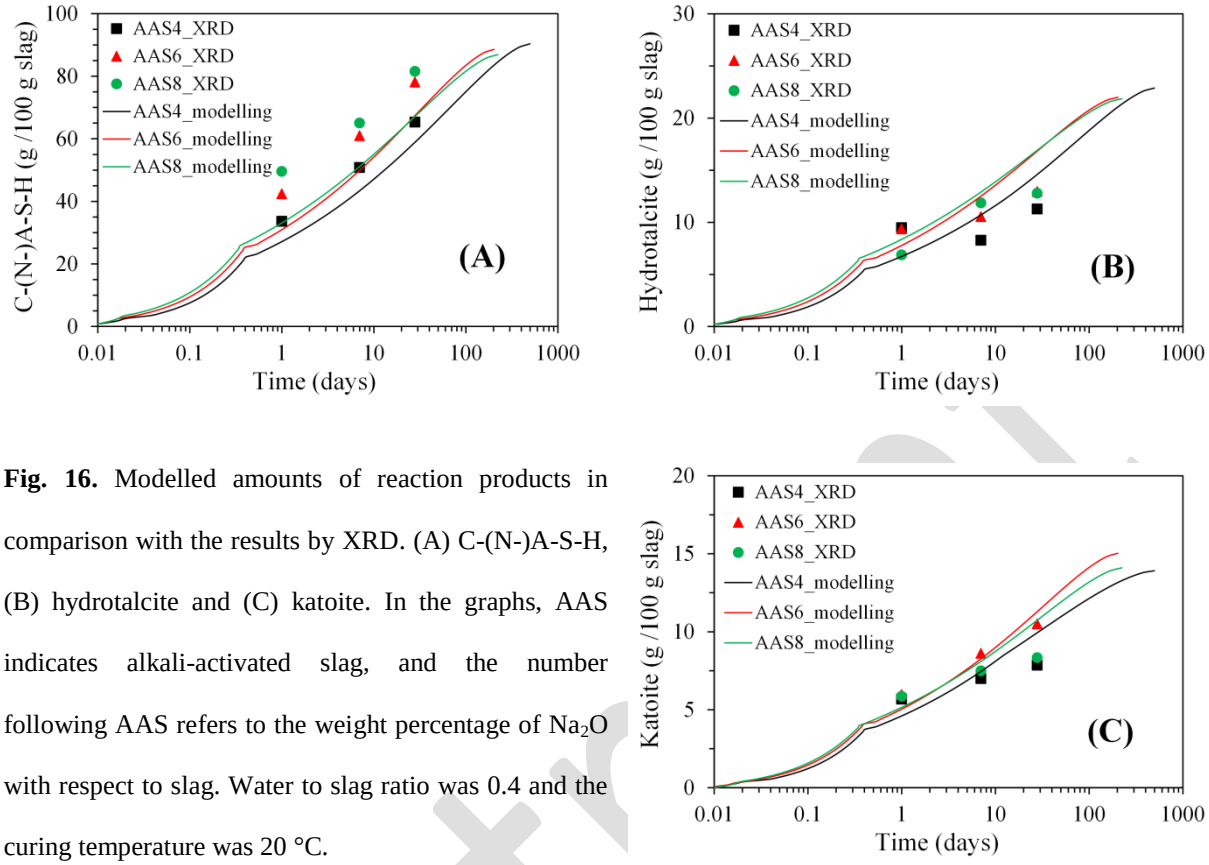

Fig. 16. Modelled amounts of reaction products in comparison with the results by XRD. (A) C-(N-)A-S-H, (B) hydrotalcite and (C) katoite. In the graphs, AAS indicates alkali-activated slag, and the number following AAS refers to the weight percentage of Na_2O with respect to slag. Water to slag ratio was 0.4 and the curing temperature was 20 °C.

3.7.4. Elemental composition of reaction products

The molar Ca/Si in C-(N-)A-S-H is reported to be typically close to 1 for alkali-activated slag [65]. Because secondary reaction products, such as C_3AH_6, C_2ASH_8 and hydrotalcite, are often intimately intermixed with C-(N-)A-S-H in alkali-activated slag [48, 49], the measured Ca/Si by SEM/EDX is influenced by the composition of reaction products in the interaction volume between the electrons and specimen. Haha et al. measured the Ca/Si to be within the range of 0.87 to 0.92 in the sodium hydroxide activated slag [9, 10], while Ye et al. measured the values to be around 1.22~1.25 [14]. Fig. 17(A) presents the atomic ratio Ca/Si as a function of time. The lines represent the Ca/Si in C-(N-)A-S-H obtained by thermodynamic modelling. The dots are the overall atomic ratio Ca/Si measured by SEM/EDX. The predicted Ca/Si in C-(N-)A-S-H by thermodynamic modelling was within 0.98~1.13 for AAS4, AAS6 and AAS8. The measured

Ca/Si by SEM/EDX was from 1.13 to 1.26. Those results are consistent with the values reported in the literature [9, 10, 14].

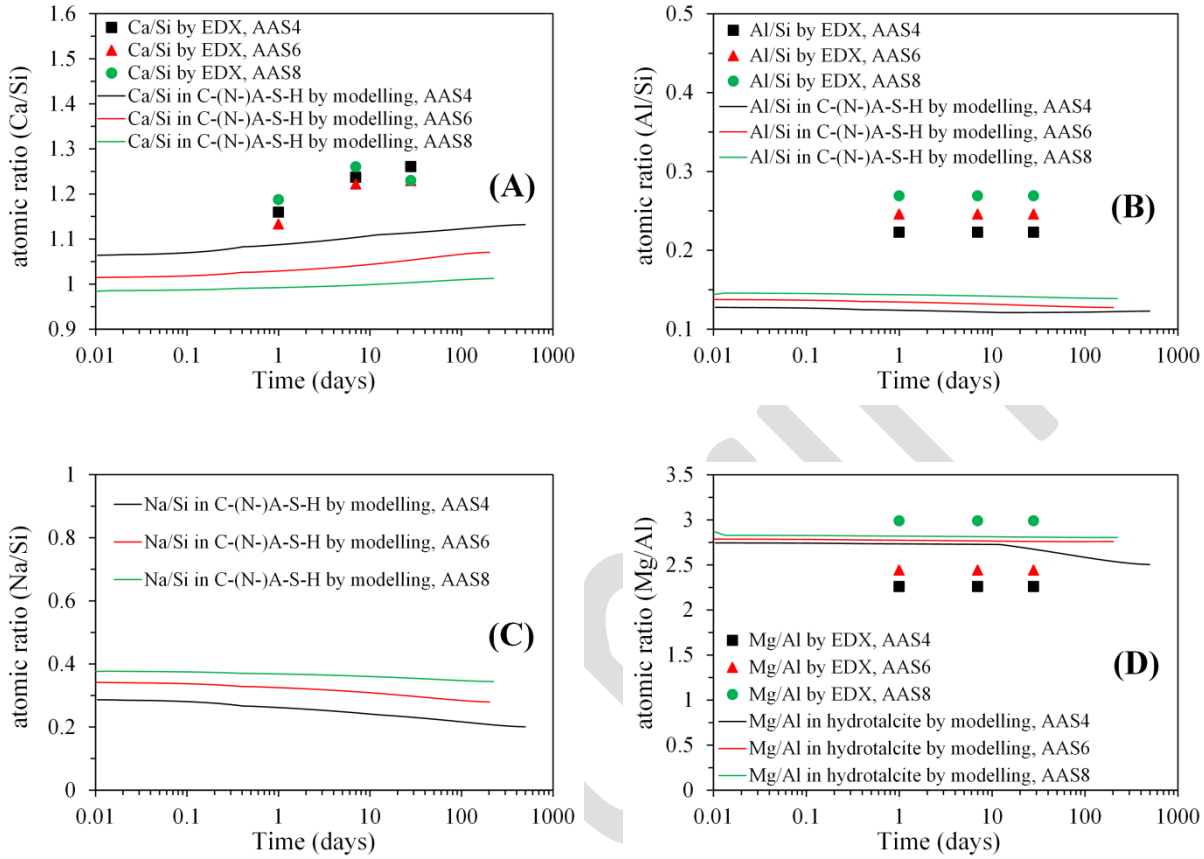

Fig. 17. Modelled atomic ratios as a function of time in comparison with the measured results. (A) Ca/Si, (B) Al/Si, (C) Na/Si and (D) Mg/Al. In the graphs, AAS indicates alkali-activated slag, and the number following AAS refers to the weight percentage of Na_2O with respect to slag. Water to slag ratio was 0.4 and the curing temperature was 20 °C.

In general, the predicted Ca/Si in C-(N-)A-S-H by thermodynamic modelling agreed with the measured Ca/Si in the altering trend with time. However, regardless of time, the predicted Ca/Si in C-(N-)A-S-H by thermodynamic modelling was always smaller than the measured Ca/Si. The relatively high values of Ca/Si measured by SEM/EDX is due to the intimately intermixed C_3AH_6 and portlandite with C-(N-)A-S-H. In the SEM/EDX microanalysis, Si was only sourced from C-

(N-)A-S-H, while Ca could be sourced from C_3AH_6 and portlandite besides C-(N-)A-S-H. As such, the extra sources of Ca led to a larger Ca/Si when compared to the Ca/Si in C-(N-)A-S-H.

Fig. 17(B) plots the atomic ratio Al/Si as a function of time. The lines represent the Al/Si in C-(N-)A-S-H obtained by thermodynamic modelling. The dots are the intercepts of the fitted lines in the Al-Si axis in Fig. 8. The measured Al/Si by SEM/EDX was within 0.22~0.27 for AAS4, AAS6, and AAS8, which matched the values reported in the literature (0.2<Al/Si<0.25) [6, 9, 10, 66]. The modelled Al/Si in C-(N-)A-S-H was larger than 0.1 and decreased slightly over time, which is consistent with previous studies [67-69]. Compared to the measured Al/Si, the predicted values by thermodynamic modelling were underestimated. The underestimation of Al/Si by thermodynamic modelling was also found in the literature [5, 12]. The modelled Al/Si in C-(N-)A-S-H increased with the increase of Na_2O content. This was attributed to the increased concentration of Al in the pore solution when increasing the content of Na_2O (see Fig. 14(B)). The increased concentration of Al in the pore solution led to increase of the uptake of Al in C-S-H [70]. In C-(N-)A-S-H, Al is mainly taken up in the bridging position of the silica dreierketten structure [67, 70, 71]. Therefore, the increase of the uptake of Al due to the increase of Na_2O content led to a larger Al/Si in C-(N-)A-S-H.

The plot of Na/Si in C-(N-)A-S-H as a function of time is presented in Fig. 17(C). A slight decrease of Na/Si in C-(N-)A-S-H can be seen as a function of time. This trend is also identified in sodium silicate and sodium carbonate activated slag systems by thermodynamic modelling [5]. When the Na_2O content in the sodium hydroxide activator increased, the Na/Si in C-(N-)A-S-H also increased. This is because the increase of Na_2O content led to higher concentration of Na in the aqueous solution of sodium hydroxide activated slag. The increased concentration of Na then resulted in higher incorporation of Na into C-S-H.

Fig. 17(D) presents the atomic ratio Mg/Al as a function of time. The lines represent the Mg/Al in hydrotalcite obtained by thermodynamic modelling. The dots are the slopes of the fitted lines in Fig. 8. As stated previously, the slope of the fitted line indicates the Mg/Al ratio in hydrotalcite [9, 10, 50]. The modelled Mg/Al in hydrotalcite matched the measured Mg/Al by EDX in the altering trends that Mg/Al increased with increase of Na_2O content and that it showed no substantial change with time except for AAS4 after 7 days. The modelled Mg/Al in hydrotalcite and the measured Mg/Al by EDX were very close and within the range of 1.92 to 4.35 reported for hydrated slag pastes [45, 51, 52], particularly for AAS8. For AAS4 and AAS6, the Mg/Al by EDX was smaller than the modelled Mg/Al in hydrotalcite. This may be attributed to the extra source of Al from katoite in addition to C-(N-)A-S-H.

4. Conclusions

The hydration of sodium hydroxide activated slag was studied by means of thermodynamic modelling and experimental techniques, such as isothermal calorimetry, ICP-OES, TGA, XRD and SEM/EDX. Based on the findings in this study, the main conclusions can be obtained as follows:

(1) On one hand, an increase of Na_2O content accelerated the reaction kinetics, led to higher elemental concentrations (except [Ca]) in the pore solution, increased the volume proportion of crystalline reaction products, and resulted in smaller chemical shrinkage at complete reaction of slag. On the other hand, the Na_2O content did not show significant influences on the type of reaction products and the ratio of the volume of reaction products relative to the volume of slag reacted.

(2) Three reaction stages were identified according to the calorimetric curves for sodium hydroxide activated slag, i.e. initial dissolution stage, acceleration/deceleration stage and steady stage. The reaction kinetics was quantified as a function of time.

(3) The hydration of sodium hydroxide activated slag, for the first time, was thermodynamically modelled in a time scale. The phase assemblage in cm^3 per 100 g of slag mixed, and chemical shrinkage were derived as a function of time.

(4) According to the evaluation of the thermodynamic modelling results in terms of pore solution composition, bound water, evolution of reaction products and elemental composition of the reaction products, the following can be concluded:

- The modelled elemental concentrations in pore solution, bound water in C-(N-)A-S-H and hydrotalcite, and evolution of reaction products matched the experimental results in the altering trend with time.
- Compared to the experimental results, the thermodynamic modelling results underestimated the elemental concentrations, but within ± 1 order of magnitude. The underestimation by thermodynamic modelling was resulted from the assumption of thermodynamic equilibriums between aqueous ions in pore solution and the solid reaction products in the modelling.
- Because the EDX microanalysis was performed over the intimately intermixed reaction products, the EDX results deviated from the atomic ratios Ca/Si and Al/Si in C-(N-)A-S-H obtained by thermodynamic modelling. However, the modelled Ca/Si and Al/Si in C-(N-)A-S-H are consistent with the observations in the literature where C-(N-)A-S-H is purely synthesized.

Acknowledgements

Microlab in Delft University of Technology is greatly appreciated and particularly the first author would like to gratefully acknowledge the China Scholarship Council (the Grant Number 201406160086).

References

[1] B. Lothenbach, D. Damidot, T. Matschei, J. Marchand, Thermodynamic modelling: State of knowledge and challenges, Adv. Cem. Res. 22(4) (2010) 211-223.
[2] D. Damidot, B. Lothenbach, D. Herfort, F.P. Glasser, Thermodynamics and cement science, Cem. Concr. Res. 41(7) (2011) 679-695.
[3] J.L. Provis, S.A. Bernal, Geopolymers and related alkali-activated materials, Annu. Rev. Mater. Res. 44 (2014) 299-327.
[4] S.-D. Wang, K.L. Scrivener, Hydration products of alkali activated slag cement, Cem. Concr. Res. 25(3) (1995) 561-571.
[5] R.J. Myers, B. Lothenbach, S.A. Bernal, J.L. Provis, Thermodynamic modelling of alkali-activated slag cements, Appl. Geochem. 61 (2015) 233-247.
[6] I.G. Richardson, A.R. Brough, G.W. Groves, C.M. Dobson, The Characterization of Hardened Alkali-Activated Blast-Furnace Slag Pastes and the Nature of the Calcium Silicate Hydrate (C-S-H) Phase, Cem. Concr. Res. 24(5) (1994) 813-829.
[7] B. Lothenbach, Thermodynamic equilibrium calculations in cementitious systems, Mater. Struct. 43(10) (2010) 1413-1433.
[8] B. Lothenbach, A. Gruskovnjak, Hydration of alkali-activated slag: thermodynamic modelling, Adv. Cem. Res. 19(2) (2007) 81-92.
[9] M.B. Haha, B. Lothenbach, G. Le Saout, F. Winnefeld, Influence of slag chemistry on the hydration of alkali-activated blast-furnace slag — Part I: Effect of MgO, Cem. Concr. Res. 41(9) (2011) 955-963.
[10] M.B. Haha, B. Lothenbach, G. Le Saout, F. Winnefeld, Influence of slag chemistry on the hydration of alkali-activated blast-furnace slag — Part II: Effect of Al2O3, Cem. Concr. Res. 42(1) (2012) 74-83.
[11] D. Kulik, J. Tits, E. Wieland, Aqueous–solid solution model of strontium uptake in C–S–H phases, Geochim. Cosmochim. Acta 71(12 Supplement 1) (2007) A530.
[12] R.J. Myers, S.A. Bernal, J.L. Provis, A thermodynamic model for C-(N-)A-S-H gel: CNASH-ss. Derivation and validation, Cem. Concr. Res. 66 (2014) 27-47.
[13] R.J. Myers, S.A. Bernal, J.L. Provis, Phase diagrams for alkali-activated slag binders, Cem. Concr. Res. 95 (2017) 30-38.
[14] H. Ye, A. Radlińska, Quantitative Analysis of Phase Assemblage and Chemical Shrinkage of Alkali-Activated Slag, J. Adv. Concr. Technol. 14(5) (2016) 245-260.
[15] R.S. Barneyback Jr, S. Diamond, Expression and analysis of pore fluids from hardened cement pastes and mortars, Cem. Concr. Res. 11(2) (1981) 279-285.
[16] K. Scrivener, T. Füllmann, E. Gallucci, G. Walenta, E. Bermejo, Quantitative study of Portland cement hydration by X-ray diffraction/Rietveld analysis and independent methods, Cem. Concr. Res. 34(9) (2004) 1541-1547.
[17] M. Ben Haha, G. Le Saout, F. Winnefeld, B. Lothenbach, Influence of activator type on hydration kinetics, hydrate assemblage and microstructural development of alkali activated blast-furnace slags, Cem. Concr. Res. 41(3) (2011) 301-310.
[18] M. Nedeljković, B. Šavija, Y. Zuo, M. Luković, G. Ye, Effect of natural carbonation on the pore structure and elastic modulus of the alkali-activated fly ash and slag pastes, Constr. Build. Mater. 161 (2018) 687-704.
[19] A. C1679-14: Standard Practice for Measuring Hydration Kinetics of Hydraulic Cementitious Mixtures Using Isothermal Calorimetry, in: (Ed.)^(Eds.), ASTM International, PA, West Conshohocken, 2014, pp.
[20] I. García-Lodeiro, A. Fernández-Jiménez, M.T. Blanco, A. Palomo, FTIR study of the sol–gel synthesis of cementitious gels: C–S–H and N–A–S–H, J. Sol-Gel Sci. Technol. 45(1) (2008) 63-72.

[21] S. Puligilla, P. Mondal, Co-existence of aluminosilicate and calcium silicate gel characterized through selective dissolution and FTIR spectral subtraction, Cem. Concr. Res. 70(0) (2015) 39-49.
[22] Z. Huanhai, W. Xuequan, X. Zhongzi, T. Mingshu, Kinetic study on hydration of alkali-activated slag, Cem. Concr. Res. 23(6) (1993) 1253-1258.
[23] A. Fernández Jiménez, F. Puertas Maroto, L. Fernández Carrasco, Procesos de activación alcalino-sulfáticos de una escoria española de alto horno, Mater Construcc 46(241) (1996) 53-65.
[24] C.J. Shi, R.L. Day, A Calorimetric Study of Early Hydration of Alkali-Slag Cements, Cem. Concr. Res. 25(6) (1995) 1333-1346.
[25] A. Khawam, D.R. Flanagan, Solid-state kinetic models: basics and mathematical fundamentals, J. Phys. Chem. B 110(35) (2006) 17315-17328.
[26] D. Ravikumar, N. Neithalath, Reaction kinetics in sodium silicate powder and liquid activated slag binders evaluated using isothermal calorimetry, Thermochim Acta 546 (2012) 32-43.
[27] A. Fernández-Jiménez, F. Puertas, Alkali-activated slag cements: kinetic studies, Cem. Concr. Res. 27(3) (1997) 359-368.
[28] C. Chen, W. Gong, W. Lutze, I.L. Pegg, Kinetics of fly ash geopolymerization, J. Mater. Sci. 46(9) (2011) 3073-3083.
[29] J.L. Provis, On the use of the Jander equation in cement hydration modelling, RILEM Technical Letters 1 (2016) 62-66.
[30] A. Ginstling, B. Brounshtein, Concerning the diffusion kinetics of reactions in spherical particles, J. Appl. Chem. USSR 23(12) (1950) 1327-1338.
[31] M. Wolthers, L. Charlet, P.R. van Der Linde, D. Rickard, C.H. van Der Weijden, Surface chemistry of disordered mackinawite (FeS), Geochim. Cosmochim. Acta 69(14) (2005) 3469-3481.
[32] D.A. Kulik, T. Wagner, S.V. Dmytrieva, G. Kosakowski, F.F. Hingerl, K.V. Chudnenko, U.R. Berner, GEM-Selektor geochemical modeling package: revised algorithm and GEMS3K numerical kernel for coupled simulation codes, Comput. Geosci. 17(1) (2013) 1-24.
[33] T. Wagner, D.A. Kulik, F.F. Hingerl, S.V. Dmytrieva, GEM-Selektor geochemical modeling package: TSolMod library and data interface for multicomponent phase models, Can. Mineral. 50(5) (2012) 1173-1195.
[34] B. Lothenbach, T. Matschei, G. Möschner, F.P. Glasser, Thermodynamic modelling of the effect of temperature on the hydration and porosity of Portland cement, Cem. Concr. Res. 38(1) (2008) 1-18.
[35] H.C. Helgeson, D.H. Kirkham, G.C. Flowers, Theoretical prediction of the thermodynamic behavior of aqueous electrolytes by high pressures and temperatures; IV, Calculation of activity coefficients, osmotic coefficients, and apparent molal and standard and relative partial molal properties to 600 degrees C and 5kb, American journal of science 281(10) (1981) 1249-1516.
[36] A. Gruskovnjak, B. Lothenbach, L. Holzer, R. Figi, F. Winnefeld, Hydration of alkali-activated slag: comparison with ordinary Portland cement, Adv. Cem. Res. (18) (2006) 119-128.
[37] K.S. Pitzer: Ion interaction approach: theory and data correlation, in: (Ed.)^(Eds.) Activity coefficients in electrolyte solutions, 1991, pp. 75-153.
[38] R.J. Myers, Thermodynamic Modelling of CaO-Al2O3-SiO2-H2O-Based Cements, PhD thesis, University of Sheffield, Sheffield, 2015.
[39] R. Snellings, Solution‐controlled dissolution of supplementary cementitious material glasses at pH 13: The Effect of Solution Composition on Glass Dissolution Rates, J. Am. Ceram. Soc. 96(8) (2013) 2467-2475.
[40] S. Ahmad, Reinforcement corrosion in concrete structures, its monitoring and service life prediction—a review, Cem. Concr. Comp. 25(4) (2003) 459-471.
[41] C. Shi, R. Day, Selectivity of alkaline activators for the activation of slags, Cement, Concrete and Aggregates 18(1) (1996) 8-14.

[42] D. Rothstein, J.J. Thomas, B.J. Christensen, H.M. Jennings, Solubility behavior of Ca-, S-, Al-, and Si-bearing solid phases in Portland cement pore solutions as a function of hydration time, Cem. Concr. Res. 32(10) (2002) 1663-1671.
[43] K. Scrivener, R. Snellings, B. Lothenbach, A Practical Guide to Microstructural Analysis of Cementitious Materials, Crc Press, 2016.
[44] F. Bonk, J. Schneider, M.A. Cincotto, H. Panepucci, Characterization by multinuclear high-resolution NMR of hydration products in activated blast-furnace slag pastes, J. Am. Ceram. Soc. 86(10) (2003) 1712-1719.
[45] H.F. Taylor, Cement chemistry, Thomas Telford, 1997.
[46] J.E. Oh, P.J.M. Monteiro, S.S. Jun, S. Choi, S.M. Clark, The evolution of strength and crystalline phases for alkali-activated ground blast furnace slag and fly ash-based geopolymers, Cem. Concr. Res. 40(2) (2010) 189-196.
[47] Y. Zuo, G. Ye, Pore Structure Characterization of Sodium Hydroxide Activated Slag Using Mercury Intrusion Porosimetry, Nitrogen Adsorption, and Image Analysis, Materials 11(6) (2018) 1035.
[48] J.I. Escalante-Garcia, A.F. Fuentes, A. Gorokhovsky, P.E. Fraire-Luna, G. Mendoza-Suarez, Hydration products and reactivity of blast-furnace slag activated by various alkalis, J. Am. Ceram. Soc. 86(12) (2003) 2148-2153.
[49] I. Richardson, G. Groves, Microstructure and microanalysis of hardened cement pastes involving ground granulated blast-furnace slag, J. Mater. Sci. 27(22) (1992) 6204-6212.
[50] M. Ben Haha, G. Le Saout, B. Lothenbach, F. Winnefeld, The hydration mechanisms of alkali activated slag systems (AAS) with different MgO content,
[51] S.-D. Wang, K.L. Scrivener, 29Si and 27Al NMR study of alkali-activated slag, Cem. Concr. Res. 33(5) (2003) 769-774.
[52] I. Richardson, Tobermorite/jennite-and tobermorite/calcium hydroxide-based models for the structure of CSH: applicability to hardened pastes of tricalcium silicate, β-dicalcium silicate, Portland cement, and blends of Portland cement with blast-furnace slag, metakaolin, or silica fume, Cem. Concr. Res. 34(9) (2004) 1733-1777.
[53] E. Altan, S.T. Erdoğan, Alkali activation of a slag at ambient and elevated temperatures, Cem. Concr. Comp. 34(2) (2012) 131-139.
[54] B.S. Gebregziabiher, R. Thomas, S. Peethamparan, Very early-age reaction kinetics and microstructural development in alkali-activated slag, Cem. Concr. Comp. 55 (2015) 91-102.
[55] T. Kishi: Thermal and mechanical modelling of young concrete based on hydration process of multi-component cement minerals, in: (Ed.)^(Eds.) Proceedings of the international RILEM symposium on Thermal Cracking in Concrete at Early Ages, Munich, Germany, 1994, 1994, pp. 11-18.
[56] K.v. Breugel, Simulation of hydration and formation of structure in hardening cement-based materials, PhD thesis, Delft University of Technology, Delft, 1991.
[57] O.M. Jensen, P.F. Hansen, Water-entrained cement-based materials: I. Principles and theoretical background, Cem. Concr. Res. 31(4) (2001) 647-654.
[58] T.C. Powers, T.L. Brownyard: Studies of the physical properties of hardened Portland cement paste, in: (Ed.)^(Eds.) Journal Proceedings, 1946, pp. 101-132.
[59] J.J. Thomas, A.J. Allen, H.M. Jennings, Density and water content of nanoscale solid C–S–H formed in alkali-activated slag (AAS) paste and implications for chemical shrinkage, Cem. Concr. Res. 42(2) (2012) 377-383.
[60] W. Chen, H. Brouwers, The hydration of slag, part 1: reaction models for alkali-activated slag, J. Mater. Sci. 42(2) (2007) 428-443.
[61] C.P. Cartwright, Shrinkage characteristics of alkali-activated slag cements, PhD thesis, The Pennsylvania State University, Pennsylvania, 2014.

[62] D. Ravikumar, N. Neithalath, Effects of activator characteristics on the reaction product formation in slag binders activated using alkali silicate powder and NaOH, Cem. Concr. Comp. 34(7) (2012) 809-818.
[63] A. Fernández-Jiménez, F. Puertas, Effect of activator mix on the hydration and strength behaviour of alkali-activated slag cements, Adv. Cem. Res. 15(3) (2003) 129-136.
[64] F. Puertas, A. Fernández-Jiménez, M.T. Blanco-Varela, Pore solution in alkali-activated slag cement pastes. Relation to the composition and structure of calcium silicate hydrate, Cem. Concr. Res. 34(1) (2004) 139-148.
[65] C. Shi, D. Roy, P. Krivenko, Alkali-activated cements and concretes, CRC press, , 2006.
[66] X. Pardal, I. Pochard, A. Nonat, Experimental study of Si-Al substitution in calcium-silicate-hydrate (C-S-H) prepared under equilibrium conditions, Cem. Concr. Res. 39(8) (2009) 637-643.
[67] R.J. Myers, S.A. Bernal, J.D. Gehman, J.S.J. van Deventer, J.L. Provis, The Role of Al in Cross-Linking of Alkali-Activated Slag Cements, J. Am. Ceram. Soc. 98(3) (2015) 996-1004.
[68] G. Le Saoût, M. Ben Haha, F. Winnefeld, B. Lothenbach, Hydration Degree of Alkali‐Activated Slags: A 29Si NMR Study, J. Am. Ceram. Soc. 94(12) (2011) 4541-4547.
[69] R.J. Myers, S.A. Bernal, R. San Nicolas, J.L. Provis, Generalized structural description of calcium–sodium aluminosilicate hydrate gels: the cross-linked substituted tobermorite model, Langmuir 29(17) (2013) 5294-5306.
[70] E. L'Hôpital, B. Lothenbach, G. Le Saout, D. Kulik, K. Scrivener, Incorporation of aluminium in calcium-silicate-hydrates, Cem. Concr. Res. 75 (2015) 91-103.
[71] R.J. Myers, J.L. Provis, B. Lothenbach, Composition-solubility-structure relationships in calcium (alkali) aluminosilicate hydrate (C-(N, K-) ASH), Dalton T (2015)